Frontiers of Physics
https://doi.org/10.1007/s11467-018-0879-7
Front. Phys.
14(3), 33401 (2019)

REVIEW ARTICLE

Local electrical characterization of two-dimensional materials with functional atomic force microscopy

Sabir Hussain[1,3], Kunqi Xu[1], Shili Ye[1,2,3], Le Lei[2], Xinmeng Liu[2], Rui Xu[1,2,†], Liming Xie[1], Zhihai Cheng[2]

[1] *CAS Key Laboratory of Standardization and Measurement for Nanotechnology, CAS Center for Excellence in Nanoscience, National Center for Nanoscience and Technology, Beijing 100190, China*
[2] *Department of Physics and Beijing Key Laboratory of Optoelectronic Functional Materials & Micro-nano Devices, Renmin University of China, Beijing 100872, China*
[3] *University of Chinese Academy of Sciences, Beijing 100049, China*
Corresponding author. E-mail: †xur@nanoctr.cn
Received September 7, 2018; accepted December 16, 2018

Research about two-dimensional (2D) materials is growing exponentially across various scientific and engineering disciplines due to the wealth of unusual physical phenomena that occur when charge transport is confined to a plane. The applications of 2D materials are highly affected by the electrical properties of these materials, including current distribution, surface potential, dielectric response, conductivity, permittivity, and piezoelectric response. Hence, it is very crucial to characterize these properties at the nanoscale. The Atomic Force Microscopy (AFM)-based techniques are powerful tools that can simultaneously characterize morphology and electrical properties of 2D materials with high spatial resolution, thus being more and more extensively used in this research field. Here, the principles of these AFM techniques are reviewed in detail. After that, their representative applications are further demonstrated in the local characterization of various 2D materials' electrical properties.

Keywords advanced AFM techniques, nanoscale characterization, electrical properties, 2D materials

Contents

1 Introduction 1
2 AFM-based electrical characterization techniques 2
2.1 Conductive-Atomic Force Microscopy (C-AFM) 2
2.2 Scanning Kelvin Probe Microscopy (SKPM) 3
2.3 Electrostatic Force Microscopy (EFM) 5
2.3.1 Conventional Electrostatic Force Microscopy (EFM) 5
2.3.2 Multi Harmonic-Electrostatic Force Microscopy (MH-EFM) 5
2.4 Scanning Microwave Microscopy (SMM) 6
2.4.1 Scanning Microwave Impedance Microscopy (sMIM) 6
2.4.2 Agilent Technology-Scanning Microwave Microscopy (AT-SMM) 6
2.5 Piezo Force Microscopy (PFM) 7
3 Electrical characterization of 2D materials 8
3.1 Current distribution investigated by Conductive-Atomic Force Microscopy (C-AFM) 8
3.2 Surface potential investigated by Kelvin Probe Force Microscopy (KPFM) 9
3.3 Application of Electrostatic Force Microscopy (EFM) 9
3.4 Application of Scanning Microwave Microscopy (SMM) 10
3.5 Piezo/ferroelectric response investigated by Piezo Force Microscopy (PFM) 11
4 Conclusion and perspectives 13
Acknowledgements 13
References 13

1 Introduction

The atomically thin two-dimensional (2D) materials are one of the most extensively studied materials, driven by continues discoveries of new physics in them [1, 2]. The single-layer graphene, known as the first stable 2D material [3, 4], exhibit unique and fascinating physical properties, such as zero-band gap [5–7], high thermal conductivity [8, 9], high carrier mobility [10, 11] and quantum hall effect [12, 13], which are highly different from its bulk. Because of these unusual properties, graphene shows promising potentials in a wide range, including nanoelectronics [14, 15], optoelectronics devices [16, 17], chemical sensor [18, 19], transparent electrodes for displays [20, 21] and

© Higher Education Press and Springer-Verlag GmbH Germany, part of Springer Nature 2019

solar cells [22, 23]. But its deficiency of an electronic band gap has enthused the search for others 2D materials with semiconducting characteristics. So far, a variety of 2D materials have been studied and new materials are still being discovered around the world [5, 24].

2D materials beyond graphene [25, 26] span the entire range of electronic structures, e.g., insulator *h*-BN [27, 28], semiconductor MoS_2, metal $NbSe_2$, and display interesting properties. *h*-BN is acknowledged as one of the ideal inert substrates to investigate intrinsic properties of atomic layers [29, 30]. MoS_2 monolayers [31, 32] can be used to prepare field effect transistor [33] and they have strong photoluminescence [34]. $NbSe_2$ layers exhibit unique properties such as superconductivity, quantum metallic state, and strong enhancement of the charge density wave (CDW) [36–38]. The great diversity of structure and remarkable properties of 2D atomic crystals make them suitable for applications in next generation of ultrathin flexible electronics [39, 40], catalyst [41, 42], chemical sensor [43, 44], lithium-ion batteries [45, 46], photo sensor device [47, 48] and field effect transistor [49, 50].

Atomic Force Microscopy (AFM) has provided a vast and valuable contribution to the understanding of the fundamental electrical properties of graphene and other 2D materials. It was invented by Nobel Prized Binnig along with his colleagues in 1986 [51]. Initially, AFM was developed to investigate the surfaces of insulators at nanoscale [52]. It obtains sample surface information by detecting the interaction forces between probe and sample other than depending on electrons or photons to detect a sample, so AFM can be applied to a wide range of systems and has predominant applications in many fields including physics, chemistry, material science and engineering.

In early period of AFM, the tip was always in mechanical contact mode with the sample surface. For instance, the first AFM image was taken by contact mode and showed nanoscale spatial resolution [52]. After a few years, Martin, Perez, and many other researchers applied dynamic operation in AFM [53–55]. The cantilever is deliberately excited at a single frequency while scanning on the sample surface [56, 57]. And a feedback loop holds one parameter of the oscillation, either the frequency or the amplitude, at a fixed value. Therefore, in the field of dynamic AFM, there are two basic methods. One is frequency modulation AFM (FM-AFM) that uses frequency as a feedback parameter and is usually operated in vacuum [58]. The other mode is amplitude modulation AFM (AM-AFM) that uses amplitude as feedback parameter and is usually operated in the atmosphere. During the last two decades, AFM and its applications have obtained broad attention from the topographic imaging to electrical mapping [59–63].

Several AFM reviews have been published to introduce the various properties of semiconductors [64, 65], material science [66], food technology [67] and biomaterials [68–70]. Considering the importance of 2D materials electrical properties, this review highlights the principles of AFM based electrical characterization methods and their further applications in 2D materials. Firstly, the principles of conductive atomic force microscopy (C-AFM), scanning Kelvin probe microscopy (SKPM), conventional electrostatics force microscopy (EFM), multiharmonic electrostatic force microscopy (MH-EFM), scanning microwave impedance microscopy (sMIM), agilent technology-scanning microwave microscopy (AT-SMM) and piezo force microscopy (PFM) are introduced in detail. Then, the applications of these techniques in characterization of the electrical properties of 2D materials are demonstrated. Finally, we summarize this review and present the prospects for new functional AFM technologies.

2 AFM-based electrical characterization techniques

Various AFM-based techniques have been developed to characterize the electrical properties of sample, such as C-AFM for current distribution or spreading resistance, SKPM for surface potential, EFM for electrostatic potential, dielectric constant or surface potential, SMM for permittivity and conductivity, and PFM for an electromechanical response. Here, the above mentioned AFM-based techniques and their applications are summarized in Table 1.

Apart from the above AFM technologies, there are many other methods to explore the electrical properties samples, such as scanning capacitance microscopy (SCM) [65] and scanning tunneling microscopy [104, 105]. Limited by the length of this review, we will focus on the methods summarized in Table 1.

2.1 Conductive-Atomic Force Microscopy (C-AFM)

C-AFM is a significant mode of AFM, which was firstly developed by Murrell and his co-workers in 1993 [106]. And now it has been referred in the literature with several names, including conductive probe AFM (CP-AFM), conductive scanning probe microscopy (C-SPM), conductive scanning force microscopy (C-SFM), and local-conductivity AFM (LC-AFM). C-AFM mode cannot only obtain current mapping of sample, but also provide I-V curve at a certain position [107]. It is sensitive in exploring the current signal of sample. Usually, the currents sensitivity can reach to nanoampere (nA).

Before describing the working principle of C-AFM, we will introduce the concept of spreading resistance. Ideally, the sample is treated as a semi-infinite uniform slab of resistivity (ρ), and tip-sample makes Ohmic contact with radius a. Then the measured resistance R will be domi-

Table 1 AFM techniques and their applications.

AFM modes	Signal of detection	Measurement of physical quantity
Conductive Atomic Force Microscopy (C-AFM)	Current	Local conductivity [71–73], defects [74, 75], dielectric breakdown [76, 77] and doping distribution [78, 79]
Scanning Kelvin Probe Microscopy (SKPM)	Electric potential	Surface potential [80–82], work function [83], charge transfer [84, 85], voltage drop [86]
Conventional Electrostatic Force Microscopy (EFM)	Electrostatic forces	Electrostatic gradient [87], surface potential [88], dielectric response [89]
Multi-Harmonic Electrostatic Force Microscopy (MH-EFM)	Electrostatic forces	Surface potential [90], work function [91], mobile charge carriers [92]
Scanning Microwave Impedance Microscopy (sMIM)	Microwave reflection	Dielectric constant [93–95], conductivity and permittivity variation [96, 97], charge carrier variations [98], doping density [99, 100]
Piezoresponse Force Microscopy (PFM)	Electromechanical coupling	Electromechanical response [81, 101], switching behavior [102], ferroelectric coercive field [103]

nated by the spreading resistance [109]:

$$R = \frac{\rho}{4a}. \tag{1}$$

During C-AFM operation, a conductive tip is placed in contact with sample surface, where the tip acts as a counter electrode [106, 108]. Then a bias voltage is applied between the conductive probe and the other counter electrode. This mode has two standard measurement geometries, as depicted in Fig. 1. Fig. 1(a) shows a vertical geometry that records the out-of-plane current distribution. Figure 1(b) shows a horizontal geometry that records the current distribution in-plane [110]. In the vertical geometry, the sample is deposited on top of a conductive substrate and the conductive tip scans over such a surface by measuring the current flowing vertically point by point. On the other hand, in a horizontal configuration, the sample is deposited on an insulating substrate and the electrical connection is obtained by laterally patterning a metal electrode. In this way, current can flow from the biased lateral contact to the moveable metal-coated scanning probe tip, and in-plane current through the material can be obtained.

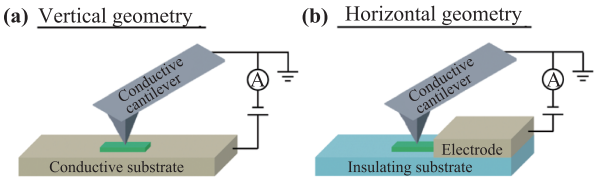


Fig. 1 The schematic diagram of the C-AFM setup. **(a)** Vertical geometry is used to measure out-of-plane current distribution through the material. **(b)** Horizontal geometry is used to measure the in-plane current distribution through the material. Reproduced with permission from Ref. [110]. Copyright © 2014 Journal of Materials Chemistry.

C-AFM enables us to study the correlation between topography and current distribution mapping. Moreover, force feedback, rather than current feedback, is used to control the tip height in C-AFM, making it possible to study surfaces with electrically insulating regions.

2.2 Scanning Kelvin Probe Microscopy (SKPM)

SKPM is a well-established AFM technique that has the capability to measure the surface potential with high lateral resolution [111]. It was invented by Nonnenmacher in 1991 [54]. This technique also has different names, such as scanning Kelvin force microscopy (SKFM) [112], Kelvin probe force microscopy (KPFM) [111] and scanning Kelvin microscopy (SKM) [113]. Recently, it has provided deep insights into the local surface potential of 2D materials [114–121].

The work function φ and contact potential difference V_{CPD} are important parameters for understanding the working principle of SKPM. The φ is defined as the energy difference between the vacuum level and the Fermi energy, as shown in Fig. 2. The V_{CPD} is defined as the difference in the φ of two materials:

$$\varphi_{\mathrm{sample}} - \varphi_{\mathrm{tip}} = \Delta\varphi = V_{\mathrm{CPD}} \cdot e. \tag{2}$$

Here $\varphi_{\mathrm{sample}}$ and φ_{tip} are the work function of sample and tip respectively, and e is the electric charge.

Figure 2(a) depicts the energy level of the tip and sample surface, when the tip and the sample are not electrically connected. The vacuum levels are associated but Fermi levels are different. Equilibrium required Fermi levels to line-up at steady state, if the tip and sample close enough for electrical contact. The Fermi energy level will align through electron current flow, and the system will achieve an equilibrium state, as shown in Fig. 2(b). If the

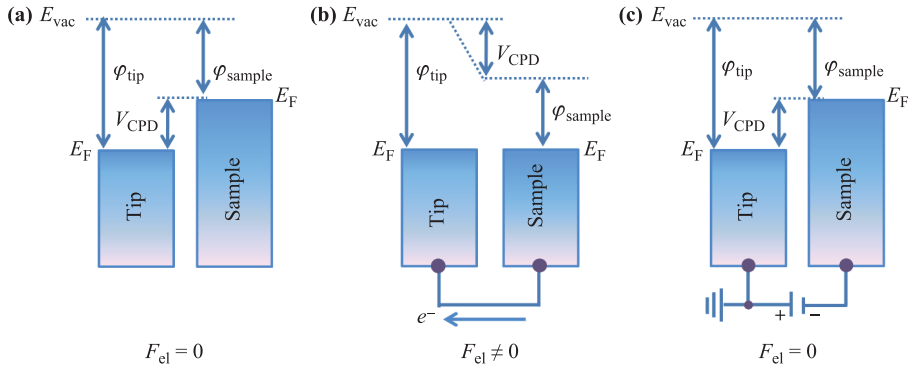


Fig. 2 Electronic energy levels between the AFM tip and sample illustrating the principle of SKPM mode. **(a)** Tip and sample are separated by a distance d with no electrical contact. They have equal E_{vac} but different E_F level. Here E_{vac} is vacuum energy level; E_F is Fermi energy level, V_{CPD} is contact potential difference and F_{el} is an electrostatic force. **(b)** Tip and sample are in electrical contact and electron transfer from the sample with higher E_F to the one with lower E_F. **(c)** By applying direct-current (DC) voltage V_{DC} ($V_{DC} = V_{CPD}$) between tip and sample, the vacuum level realigns.

applied V_{DC} has the same magnitude as the V_{CPD} and opposite sign of it, the applied voltage eliminates the F_{el}, as shown in Fig. 2(c). Hence, the V_{CPD} can be measured by SKPM, thereby the work function of sample can be obtained when the tip work function is known.

Figures 3(a) and (b) demonstrate that SKPM is performed in two passes (nap mode) to explore the surface potential of sample. In the first pass, the topography can be obtained same as standard AC mode (tapping mode) [114, 115]. In the second pass, the tip is raised above the sample surface by lift mode. The mechanical excitation is switched off, and then V_{DC} and V_{AC} [116] are applied between the tip and sample [117]. The electrostatic force between tip and sample is given by

$$F_{el} = \frac{1}{2}\frac{\partial C}{\partial z}\Delta V^2. \tag{3}$$

Here, $\frac{\partial C}{\partial z}$ and ΔV are the capacitance coupling and voltage difference between AFM tip and sample respectively. The total voltage difference between the tip and the sample is

$$\Delta V = (V_{DC} - V_{CPD}) + V_{AC}\sin(\omega_e t), \tag{4}$$

where ω_e is the angular frequency of the applied AC voltage. Then the electrostatic force applied to the AFM tip:

$$F_{el} = \frac{1}{2}\frac{\partial C}{\partial z}\left(\left[(V_{DC} - V_{SP})^2 + \frac{1}{2}V_{AC}^2\right] + 2[(V_{DC} - V_{CPD})V_{AC}\sin(\omega_e t)] - \left[\frac{1}{2}V_{AC}^2\cos(2\omega_e t)\right]\right), \tag{5}$$

where

$$F_{\omega_e} = \frac{\partial C}{\partial z}[V_{DC} - V_{CPD}]V_{AC}\sin(\omega_e t). \tag{6}$$

In order to get higher signal-to-noise ratio, researchers generally set ω_e equals to ω_r (which means $F_{\omega_r} = F_{\omega_e}$) in SKPM mode. If F_{ω_r} reaches minimum, the V_{CPD} can be acquired which shows the local surface potential of sample [118, 119].

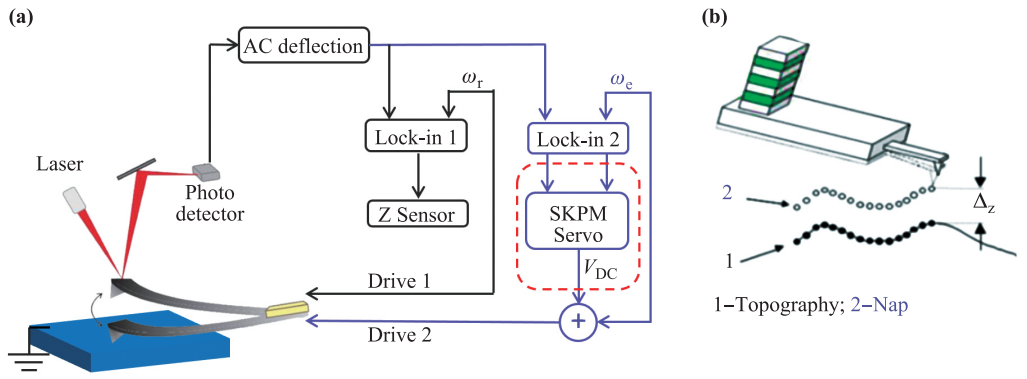


Fig. 3 **(a)** Schematic of the basic setup for SKPM. **(b)** Sketch map of two scan passes. In the first scan, the topography is acquired using mechanical excitation of the cantilever. In the second scan, the surface potential is acquired. The electronic circuit diagram of first scan and second scan are plotted by black and blue lines respectively. Where ω_r is the resonant angular frequency of cantilever; ω_e is the angular frequency of the applied AC voltage.

2.3 Electrostatic Force Microscopy (EFM)

Up to now EFM technology has many branches [120], such as conventional EFM [124–128], MH-EFM [121, 122] and dynamic contact EFM (DC-EFM) [123]. Through recording long-range electrostatic forces between tip-sample, EFM can measure the electric field gradient distribution, and allow the extraction of capacitance changes, distribution of electrical potential and embedded conductor of sample. In this review, we are going to introduce the principles of conventional EFM [124–128] and MH-EFM in detail [121, 122].

2.3.1 Conventional Electrostatic Force Microscopy (EFM)

A general illustration of the principle of conventional EFM is shown in Figure 4. Conventional EFM operates in two-pass processes, also known as lift-mode. In the first scan, the topography image can be obtained same as standard tapping mode[130]. In the second scan, the tip is raised up (by lift mode) to a controllable height z above the sample surface at a specific distance (usually z is about 20–50 nm). Meanwhile, V_{DC} is applied between the tip and sample in lift mode, phase shift of the cantilever oscillation is monitored to explore the electrostatic gradient of sample [131, 132].

2.3.2 Multi Harmonic-Electrostatic Force Microscopy (MH-EFM)

MH-EFM is a newly-developing powerful EFM mode that uses multi-frequency for the characterization of electrical properties [90, 133–135]. Different from the conventional EFM, it has the ability to quantitative/semi-quantitative measure the various physical quantities, such as carrier type and carrier concentration.

To describe the working principle of MH-EFM, it is important to understand the effect of frequency on the capacitance–voltage (C–V) curve, as shown in Fig. 5. Figure 5(a) shows schematic of ideal metal-insulator-semiconductor (MIS) structure. Here we use p-type silicon as an example. Figure 5(b) shows the C–V curves of p-type silicon under different frequency. From the C–V curves, the carrier concentration and carrier type can be obtained [10].

In MH-EFM, dual pass mode was used to detect topography and electrical properties of sample. In the first pass, the AFM works the same way as the typical AC mode (tapping mode) [122]. In second pass (lift mode), a V_{AC} with a frequency of $f_{\omega e}$ is applied between the tip and sample, resulting in multi-harmonic electrostatic force [58, 137]. The electrical force is as follows [121]:

$$\begin{aligned} F_{\mathrm{el}} = -\frac{1}{4}\Bigg\{ & \frac{\partial C}{\partial z}V_{\mathrm{AC}}^2 + \frac{\partial^2 C}{\partial V \partial z}V_{\mathrm{AC}}^3 \cos(\omega_{\mathrm{e}} t) \\ & + \frac{\partial C}{\partial z}V_{\mathrm{AC}}^2 \cos(2\omega_{\mathrm{e}} t) \\ & + \frac{1}{2}\frac{\partial^2 C}{\partial V \partial z}V_{\mathrm{AC}}^3 [\cos(3\omega_{\mathrm{e}} t) + \cos(\omega_{\mathrm{e}} t)] \Bigg\}. \end{aligned} \tag{7}$$

Accordingly, the second and third harmonic components are given by

$$F_{2\omega_{\mathrm{e}}} = -\frac{1}{4}\frac{\partial C}{\partial z}V_{\mathrm{AC}}^2 \cos(2\omega_{\mathrm{e}} t), \tag{8}$$

$$F_{3\omega_{\mathrm{e}}} = -\frac{1}{8}\frac{\partial^2 C}{\partial V \partial z}V_{\mathrm{AC}}^3 \cos(3\omega_{\mathrm{e}} t). \tag{9}$$

The $\frac{\partial C}{\partial z}$ and $\frac{\partial C}{\partial V}$ can be obtained by detecting the $2\omega_{\mathrm{e}}$ and $3\omega_{\mathrm{e}}$ components. In another word, the $A_{2\omega}$ and $A_{3\omega}$

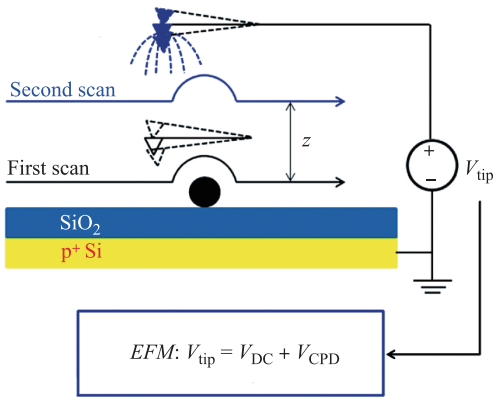


Fig. 4 Schematic diagram of conventional EFM. In the first scan, the topography can be obtained by standard AC mode. In the second scan (lift mode), electrostatic gradient distribution of sample can be obtained. Reproduced with permission from Ref. [129]. Copyright © 2013 Journal of Materials Chemistry.

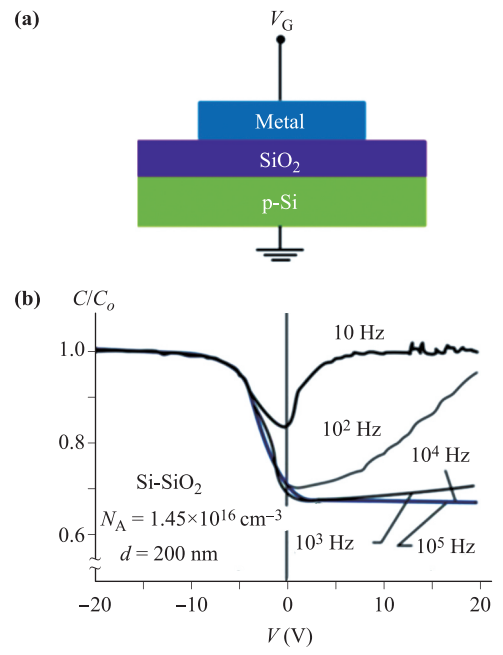


Fig. 5 The effect of frequencies on the C–V curve. **(a)** The schematic of the ideal MIS structure. The p-type silicon is used as an example. **(b)** Effect of frequencies on C–V curve. Reproduced with permission from Ref. [136].

can reflect the dielectric constant (or capacitance) and carrier concentration of the sample surface, respectively [90, 134, 138]. Furthermore, this method is not affected by stray capacitance.

2.4 Scanning Microwave Microscopy (SMM)

Scanning microwave microscopy (SMM) is a technique which combines of microwave technology and AFM. It is a tool for the investigation of various properties of 2D material, which including conductivity, permittivity, impedance etc. at nanoscale. SMM has received extensive attention and has many branches recently, such as scanning microwave impedance microscopy (sMIM), agilent-technology scanning microwave microscopy (AT-SMM) and interferometric scanning microwave microscopy (iSMM). In this review, we are going to introduce the principles of sMIM and AT-SMM in detail because they are more widespread popularity than iSMM.

2.4.1 Scanning Microwave Impedance Microscopy (sMIM)

sMIM is a quantitative near-field tool [139, 140] that operates at high frequency ~GHz range [140] and can detect the electrical properties of various samples, including conductors, semiconductors, insulators, and other functional materials at macro/nano scale. Currently, it has been widely used to explore the electrical properties of 2D materials such as conductivity, permittivity [96, 97], charge carrier variations, doping density and dielectric constant [94, 96, 97, 141–143].

During sMIM operation, a microwave signal at high frequency (few gigahertzes) is applied into tip apex, as shown in Fig. 7, and then this signal is transmitted to sample

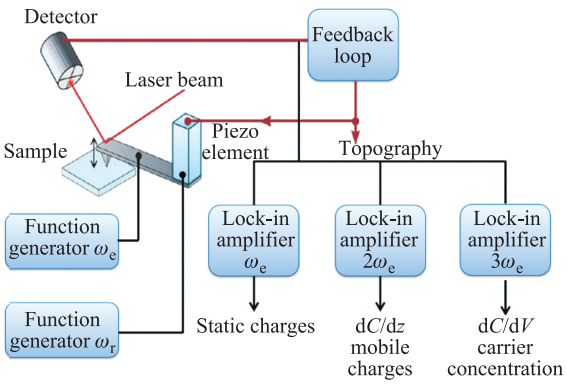


Fig. 6 Schematic diagram of MH-EFM mode. A cantilever was driven by the output of a PLL circuit (drive frequency f_{ω_e}). The amplitude of cantilever vibration at $f_{\omega e}$, $f_{2\omega e}$ and $f_{3\omega_e}$ are obtained by Lock-in amplifier, named as A_ω, $A_{2\omega}$, and $A_{3\omega}$. A_ω is proportional to surface potential, $A_{2\omega}$ has relation with dielectric constant, while amplitude $A_{3\omega}$ is corresponding to carrier concentration of the sample. Reproduced with permission from Ref. [135]. Copyright © 2018 Journal of IOP.

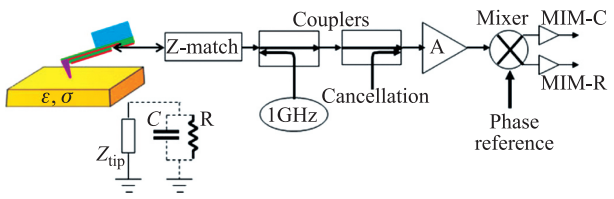


Fig. 7 Depiction of the experimental set up for sMIM. The reflected microwave resolves by RF mixer into MIM-Im and MIM-Re channel, which are related to conductivity and permittivity of sample. The inset shows the equivalent lumped element circuit of the tip-sample interaction. The sMIM can perform both in contact mode and AC (tapping) mode. Reproduced with permission from Ref. [144]. Copyright © 2011 Journal of Applied Nanoscience.

[139, 140, 145]. As the microwave signal strikes on the sample surface, some of the microwave signals are reflected from the sample surface and some pass through. The reflection coefficient Γ of microwave signals from the contact point to measure the tip-sample impedance mismatch can be written as

$$\Gamma = \frac{Z_{\text{tip-sample}} - Z_0}{Z_{\text{tip-sample}} + Z_0}. \tag{10}$$

Here, $Z_{\text{tip-sample}}$ and Z_0 are tip-sample impedance and characteristic impedance of the transmission line system, respectively [139]. Thus, the reflected signal is suppressed by the common-mode cancellation through directional couplers so that small changes can be amplified by the amplifier (A) without saturating the output. Finally, reflected signals resolve by radio frequency mixer (RF mixer) into MIM-Im and MIM-Re, as shown in Fig. 7 [146]. For semiconductors or insulators, the MIM-Im and MIM-Re are corresponding to the capacitance (C) and resistance (R) between tip-sample respectively, as shown in the insert image lumped element model. Furthermore, the $\mathrm{d}C/\mathrm{d}V$ and $\mathrm{d}R/\mathrm{d}V$ can be obtained when another modulation voltage is applied to sample [144].

2.4.2 Agilent Technology-Scanning Microwave Microscopy (AT-SMM)

Except sMIM, agilent technology put forward the AT-SMM mode, which consists of AFM and a vector network analyzer (VNA), as depicted in Fig. 8. It has been designed to exploit the flexibility and outstanding accuracy of a vector network analyzer (VNA) to measure impedance [147]. It is also possible to engineer the SMM to determine differential capacitance ($\mathrm{d}C/\mathrm{d}V$) [148].

During AT-SMM, an RF cable is connected between VNA and conductive AFM-tip. A microwave signal is injected from VNA to AFM-tip, and then this signal is transmitted to the sample. As the microwave signals strike on the sample surface, some of the microwave signals are reflected and some pass through the sample surface. Then the reflected signal from the tip is detected by VNA again.

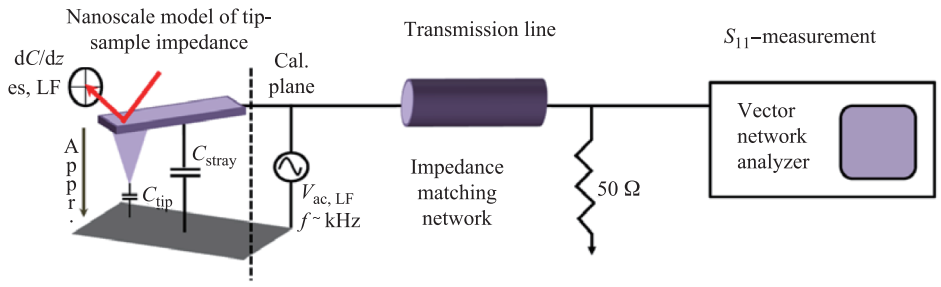


Fig. 8 Schematic diagram of AT-SMM setup. The conductive AFM-tip is contacted to a VNA by a transmission line and impedance matching network. The VNA is microwave emitter and detector. Reproduced with permission from Ref. [149].

Copyright © 2014 Journal of IOP.

To reduce impedance mismatch, there is a transmission line resonator between the probe and the 50Ω resistor splitter, allowing only specific frequency microwave passes through [149–151].

2.5 Piezo Force Microscopy (PFM)

Piezoelectric materials, which respond mechanically to applied electric field and vice versa, are essential for electromechanical transducers. The fundamental electromechanical response of these material has been investigated by PFM [152–154], which was invented by P. Guthner and K. Dransfeld in 1992 [155]. Up to now, PFM has given valuable contribution to explore the ferro/piezoelectricity response of 2D piezoelectric materials. [81, 156, 163].

In PFM, the conductive tip is brought in contact with the sample surface [159–161], as shown in Fig. 9. Meanwhile, V_{AC} with driving frequency ω is applied between tip and back electrode of the sample [157, 162],

$$V_{tip} = V_{DC} + V_{AC}\cos(\omega t). \tag{11}$$

Then the deflection induced by V_{AC} at the ω is obtained by a lock-in amplifier. Hence, the electromechanical response of sample is detected as the first-harmonic component ($A_{1\omega}$) of biased induced tip deflection:

$$d = d_0 + A_{1\omega}\cos(\omega t + \varphi_0), \tag{12}$$

Where d is the tip deflection response that describes the local electromechanical response and d_0 represents the deflection of the set point [35]. Meanwhile, the phase φ_0 provides yield information about the polarization underneath the tip. For c^- domains (polarization vector oriented normal to the surface and pointing downward), the application of a positive tip bias results in the expansion of the sample, which means $\varphi_0 = 0$. For c^+ domains, the response is opposite and $\varphi_0 = 180°$.

But there is difficulty in the acquisition of PFM signals from non-negligible electrostatic interactions between the tip and the surface [164–166]. In the general case, the measured amplitude of the piezoresponse can be written as

$$A = A_{el} + A_{piezo} + A_{nl}, \tag{13}$$

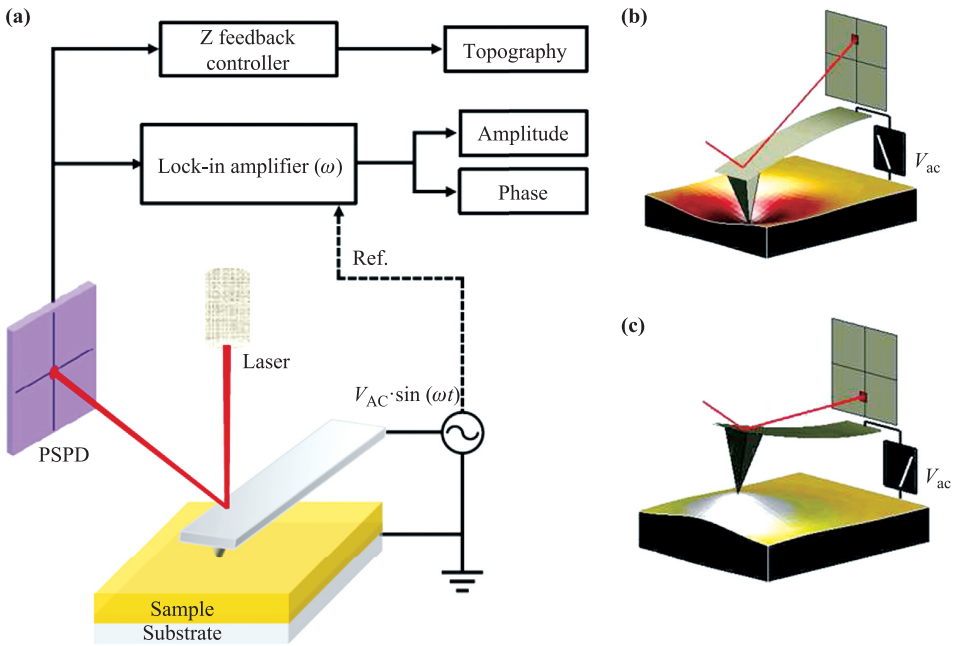


Fig. 9 Schematic diagram of the PFM technique. **(a)** The conductive tip is brought in contact with the sample surface. V_{AC} is applied between the conductive cantilever and sample. Then the electromechanical mapping is measured by detecting the first-harmonic component $A_{1\omega}$. Reproduced with permission from Ref. [157]. Copyright © 2017 Journal of Current Applied Physics. **(b, c)** The sample deforms in response to the applied voltage. This, in turn, causes the cantilever to deflect, which can then be measured and interpreted in terms of the piezoelectric properties of the sample. Reproduced with permission from Ref. [158].

where A_{el}, A_{piezo} and A_{nl} are the amplitudes of electrostatic contribution, electromechanical contribution and nonlocal contribution due to capacitive cantilever-surface interaction respectively [167]. Quantitative PFM mapping requiresA_{piezo} to be maximized to accomplish electromechanical contrast. Except the real space imaging of piezoelectric coefficient (d_{33}), the displacement-voltage and d_{33}–V curves can also be obtained in PFM mode.

The usage of above techniques requires the users not only have clear physical concepts, but also are familiar with electronic circuit design. We believe one can choose and use appropriate methods to start their study after reading above section. The application of AFM-based electrical characterization of 2D materials is an emerging field. In the following part, we will introduce recent studies of local electrical characterization of 2D materials with these AFM methods.

3 Electrical characterization of 2D materials

3.1 Current distribution investigated by Conductive-Atomic Force Microscopy (C-AFM)

C-AFM is a powerful technique for studying the spatial variability of electronic properties of materials at nanoscale through the current measurement. Many researchers have described that this tool can be used to detect the topography and current distribution between respective layers of few-layers 2D materials.

Figures 10(a) and (b) show the topography and current mapping of rGO on SiO_2 by C-AFM. The defective regions (marked by 1) are far more easily visualized in the current channel than in the topography. In Fig. 10(c), the local I–V curves reveal currents over monolayer regions are 3.9 ± 0.5 times smaller than the currents over multilayer regions. By considering the stacked rGO layers as an approximation of parallel conductors, they claim that the current per layer in the multilayer is 1.3 times larger than the current in the monolayer. It shows that the current density of rGO depends on their thickness and defects concentration [168].

Furthermore, the current distribution in other 2D materials has also been investigated by C-AFM, such as defective monolayers WS_2 [75], MoS_2 and WSe_2 after immersion in solvents [175, 176]. Here, the topography and current mapping of h-BN flakes on gold-coated mica substrate are shown in Figs. 10(d–f) [169] in detail. The profile lines in Figs. 10(d–f) depict the changes of thickness and current of h-BN. They conclude that current is a function of thickness, as predictable, and that the insulation quality is uniform within the areas of the same thickness. These results confirm that h-BN is the most perfect candidate for ultrathin insulator.

Through detecting the current signal, numerous properties of 2D materials can also be obtained. For instance, dielectric breakdown in h-BN layers [170, 171], local conductivity in heterostructure of MoS_2/WS_2 and graphene oxide [172, 173], contact resistivity between the heterostructure of MoS_2/GaN [174] and so on.

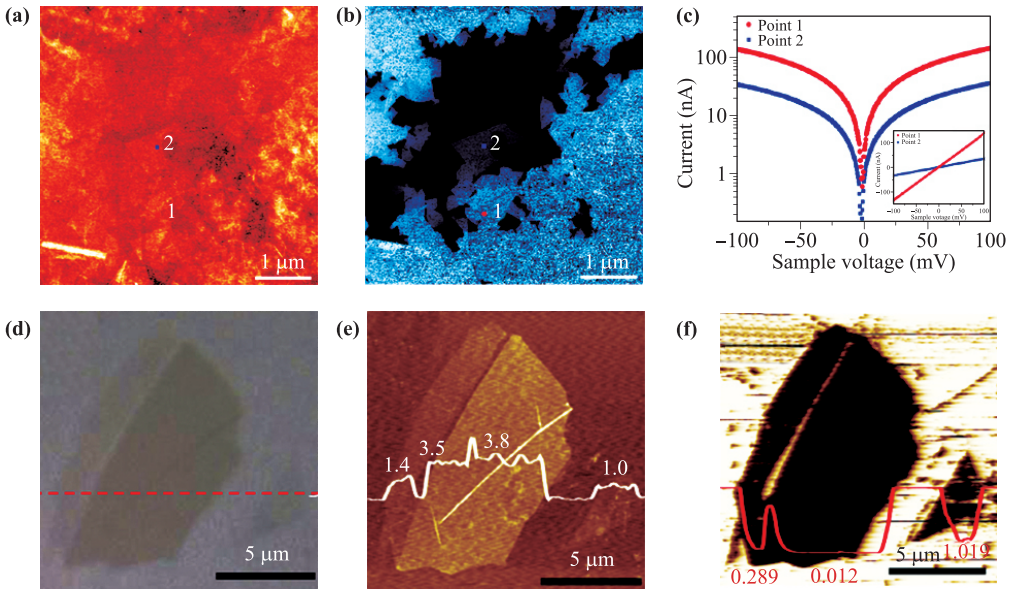


Fig. 10 Current distribution in 2D materials studied by C-AFM. **(a, b)** The (a) topography and (b) current mapping of reduced graphene oxide (rGO) sheets taken in contact mode. **(c)** Current–voltage (I–V) curves obtained at single and three layers of rGO locations. Reproduced with permission from Ref. [168]. Copyright © 2010 Journal of American Chemical Society. **(d–f)** The (d) optical image, (e) topography and (f) current images of mechanical exfoliation h-BN flakes with different thickness, respectively. Reproduced with permission from Ref. [169]. Copyright © 2011 Journal of Applied Physics Letters.

3.2 Surface potential investigated by Kelvin Probe Force Microscopy (KPFM)

KPFM has advantages in quantitative measurement of surface potential of sample, and it provides countless studies about 2D materials recently [80, 177–184]. Figures 11(a) and (b) show topography and surface potential (and/or work function) images of multilayers MoS_2 investigated by KPFM. [177] Surface potential of MoS_2 flakes with different layers thickness is demonstrated. It is known that the larger (smaller) surface potential means lower (higher) work function and the higher (lower) Fermi surface. Thus surface potential of SiO_2 is lager (work function is lower) than MoS_2. The surface potentials of MoS_2 depend on the thickness of the layer. The thicker the MoS_2 is, the smaller the surface potential is. For instance, the surface potential of monolayer and three-layers MoS_2 are -95 mV and -240 mV respectively. Additionally, surface potential [81, 181–198] of other 2D materials have also been studied, which we would not introduce in detail here.

Except 2D materials, the van der Waals heterostructures are investigated by several groups [82]. Here, the surface potential of MoS_2 (monolayer)/WS_2 (multilayer) (abbreviated as WS_2/MoS_2) heterostructure on SiO_2/Si substrate is introduced as an example [178]. Electrical transport studies demonstrate that the special MoS_2/WS_2 serves as intrinsic lateral p-n diodes, and depletion-layer width and built-in potential are obtained by KPFM. Figures 11(d) and (e) show AFM topography and surface potential images of low-pressure CVD grown MoS_2/WS_2 heterostructure. The Fermi levels of WS_2 or MoS_2 in the heterostructure can be estimated from value of their surface potential. Figure 11(f) shows profile of surface potential along the blue dash line in Figure 11(e). According to this section line, the built-in potential ∼95 mV and the depletion-layer width W ∼3.84 μm are obtained.

Furthermore, through monitoring the surface potentials, micro mechanisms of some phenomenon have been studied by different groups [179, 199–201]. Verdaguer *et al.* have characterized the discharging of graphene induced by water in controlled ambient conditions [199]. Zhou *et al.* have explored the contact electrification process both in polarity and magnitude of the charge transfer through an applied electric field between two materials [200]. We confirm the SKPM method will provide more help in understanding the electrical properties in the future.

3.3 Application of Electrostatic Force Microscopy (EFM)

EFM is also a crucial mode to study the electrical properties of sample. It can be used not only in detecting the electronic perturbations, domains and/or atomic defects of materials, but also in understanding the underlying work mechanisms of nanodevices [89, 202–205].

Datta *et al.* employed EFM to explore the electrostatic potential and charge distribution in few-layer graphene (FLG) on SiO_2/Si substrate grown by mechanical exfo-

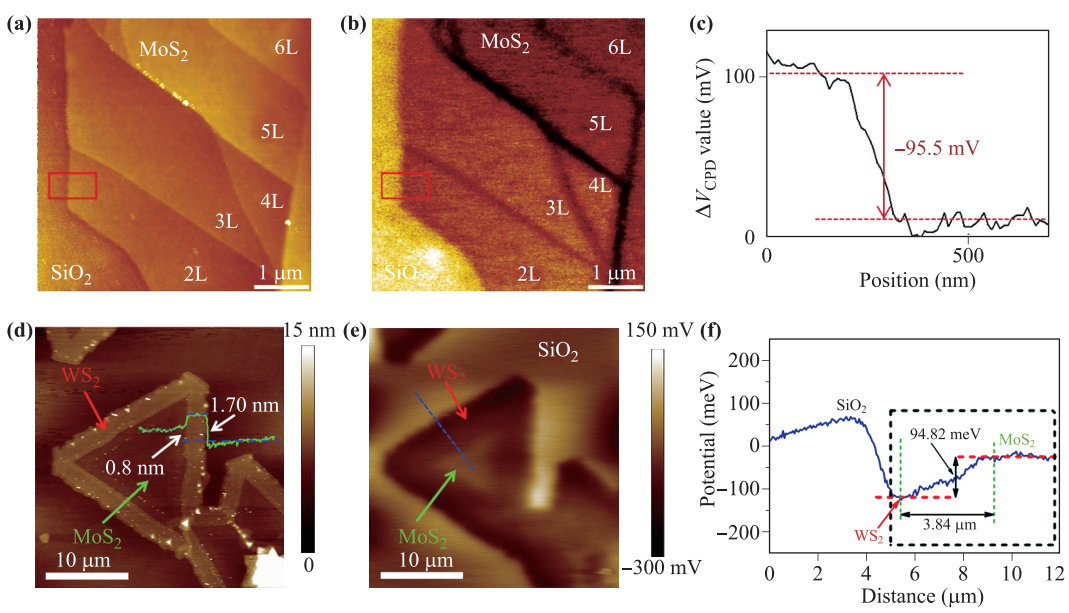


Fig. 11 Surface potential of MoS_2 few layers and WS_2/MoS_2 heterostructure characterized by KPFM. **(a, b)** The AFM (a) topography and (b) corresponding surface potential image of mechanical exfoliation multilayer MoS_2 on SiO_2/Si substrate taken in KPFM mode. The brighter region in (b) means larger surface potential. **(c)** Line profile of potential difference recorded along the red square line plotted in (b). Reproduced with permission from Ref. [177]. Copyright © 2014 Journal of the Korean Physical Society. **(d, e)** The AFM (d) topography and (e) surface potential image of the WS_2/MoS_2 heterostructure taken in KPFM mode. **(f)** Line profile of the surface potential recorded along the blue dash line in (e). Reproduced with permission from Ref. [178]. Copyright © 2015 Journal of ACS Nano.

liation method [88]. Figures 12(a) and (b) demonstrate the topography of FLG with different thickness and their corresponding EFM mapping. FLG regions with different numbers of graphene layers exhibit different values of phase shift $\Delta\Phi$, as shown in Fig. 12(c). Furthermore, local surface potential V_{SP} of sample can be quantified by measuring phase shift $\Delta\Phi$ as a function of V_{tip}, as shown in Fig. 12(d). They reported that the FLG surface potential increases with film thickness, approaching a bulk value for samples with five or more graphene layers.

The EFM can also be used to elucidate the work mechanism in device. Sangwan *et al.* have studied the switching mechanism in memristor device of MoS_2 on SiO_2/Si substrate [203]. Figure 12(e) shows the AFM phase image of an electroformed bisecting-Grain Boundary (GB) device. It shows the GB (highlighted by a black arrow) divides the channel into two regions connected to drain and source electrodes. Figures 12(f–h) show corresponding EFM images of MoS_2 device with different tip biases. The abrupt change of the phase across a bisecting-grain boundary indicates that electrostatic potential drop occurs primarily at the grain boundary. This confirms the overall higher resistance of the bisecting-GB memristor compared to the bridge-GB memristor. Furthermore, the switching mechanism of devices with GBs is obtained with the help of EFM.

The MH-EFM is also a promising tool for quantitative characterization of 2D materials with nanometer resolution [90]. Collins *et al.* employed MH-EFM (DH-KPFM) to explore the surface potential of CVD grown monolayer graphene on Cu foil substrate. First harmonic response demonstrates a clear contrast in charge density between graphene and substrate. Meanwhile, second harmonic response depicts the contrast consistent with changes in the capacitance gradient associated with changes in the probe-sample capacitor geometry. The surface potential was determined to be 157 ± 9 mV and -47 ± 5 mV, for the tip-graphene and tip-Cu interactions respectively, shown in Fig. 13(c). Then the relative surface potential difference between the graphene and Cu can be obtained, which is 204 ± 10 mV [134].

Recently, Lei *et al.* employed MH-EFM to explore the mobile charge carrier of MoS_2 on SiO_2 with circle holes arrays [135]. They describe the $A_{3\omega}$images of MoS_2 with different gate voltages V_G [206]. The $A_{3\omega}$ contrast of whole MoS_2 is uneven, which confirms the difference of carrier concentration in MoS_2 flakes. The buried holes can also be observed, which indicate that the MH-EFM has subsurface scanning ability (penetration depth in $MoS_2 \sim 75$ nm).

Up to now, several groups have employed EFM to investigate other 2D materials, such as charge injection in reduced graphene oxide [207], dielectric response of h-BN layers [89], surface potential of few-layer graphene [208, 209], capacitance behavior of graphene [210, 211], electrostatic properties of MoS_2 [212, 213] and so on.

3.4 Application of Scanning Microwave Microscopy (SMM)

SMM is a quantitative near-field tool that operates at high frequencies in the GHz range and can detect the local

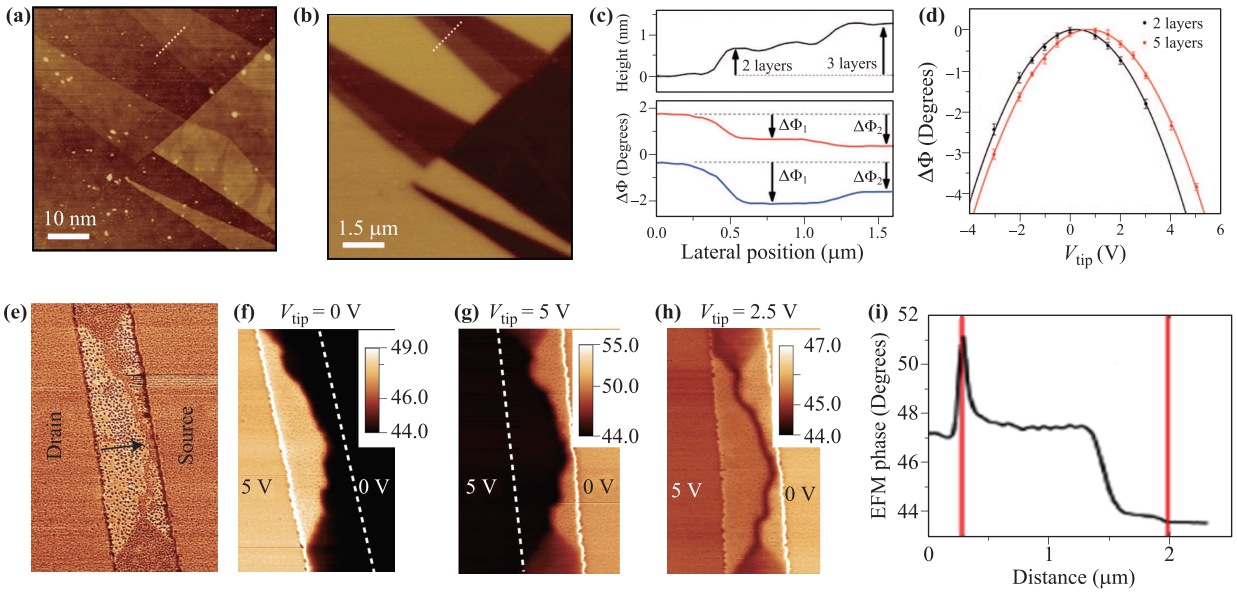


Fig. 12 Few-layers graphene (FLG) and monolayer MoS_2 device characterized by EFM. **(a, b)** Topography and EFM (phase) images of FLG. **(c)** Line profile of topography and phase image along the white dash lines in (a, b). **(d)** EFM phase shift versus tip voltage for FLG with 2 or 5 layers (black and red data respectively). Reproduced with permission from reference [88]. Copyright © 2009 Journal of Nano Letters. **(e)** AFM phase image of an electroformed bisecting-GB device. **(f–h)** The corresponding EFM images of MoS_2 device at different tip biases. **(i)** Line profile of phase image along the black arrow in (e). Reproduced with permission from Ref. [203]. Copyright © 2015 Journal of Nature Nanotechnology.

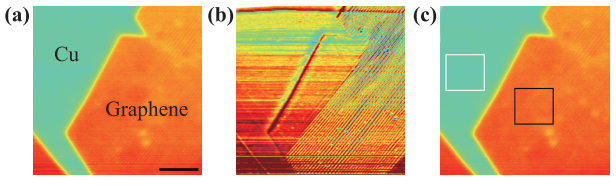


Fig. 13 Single-layer Graphene characterized by MH-EFM. **(a, b)** First and second harmonic response of single-layer graphene. **(c)** Corresponding surface potential image. Reproduced with permission from reference [134]. Copyright 2014 Journal of Applied Physics Letters.

changes of various properties of 2D materials [94, 96, 97, 141, 142]. Kundhikanjana *et al.* employed sMIM to explore the conductivity of graphene flakes and its derivatives on SiO_2/p++Si substrate. The MIM-Im signal of PG sample is brighter than substrate due to higher conductivity, while its MIM-Re images show homogeneous contrast, as shown in Figs. 14(a) and (b). Using the finite-element analysis (FEA), they claim that conductivity of PG is $\sigma > 10^6$ S/m. Whereas AGO pieces appear darker in MIM-Im images [Fig. 14(c)], which indicates the conductivity of AGO is 10–100 S/m. Moreover, the experiment data and simulation conductivity of other derivatives are shown in Fig. 14(e). The results show GO, RGO and AGO are low conductivity, while PG, AGS and GS are high conductivity [97].

In addition to above material classification, sMIM can also provide help in study of 2D materials thermal oxidation mechanism. It is known that the fully oxidized products is WO_3, however the oxidation process is not well understood. Liu *et al.* used sMIM to characterize thermal oxidation process of mechanically exfoliated WSe_2 layers on SiO_2/Si substrate. Figures 14(f–h) shows that AFM topography and sMIM mapping was obtained simultaneously from the same region. sMIM mapping exposes that the electrical conductivity is higher in certain region of the sample. The theoretical analysis in Fig. 14(i) indicates that these bright areas correlate with the intermediate product WO_{3-x} in the oxidation process [96].

What's more, local conductivity of several 2D materials has been further investigated by SMM, such as MoS_2, black phosphorous, WS_2 and graphene [141, 142, 147, 214–216]. Besides that, dielectric constant of In_2Se_3 and MoS_2 [94, 95], local permittivity of multi layers phosphorene [217] and local impedance of graphene [218] have also been studied recently.

3.5 Piezo/ferroelectric response investigated by Piezo Force Microscopy (PFM)

PFM is a powerful tool for investigating ferroelectric and piezoelectric materials at nanoscale. Recently, it has been used to detect the electromechanical response of 2D mate-

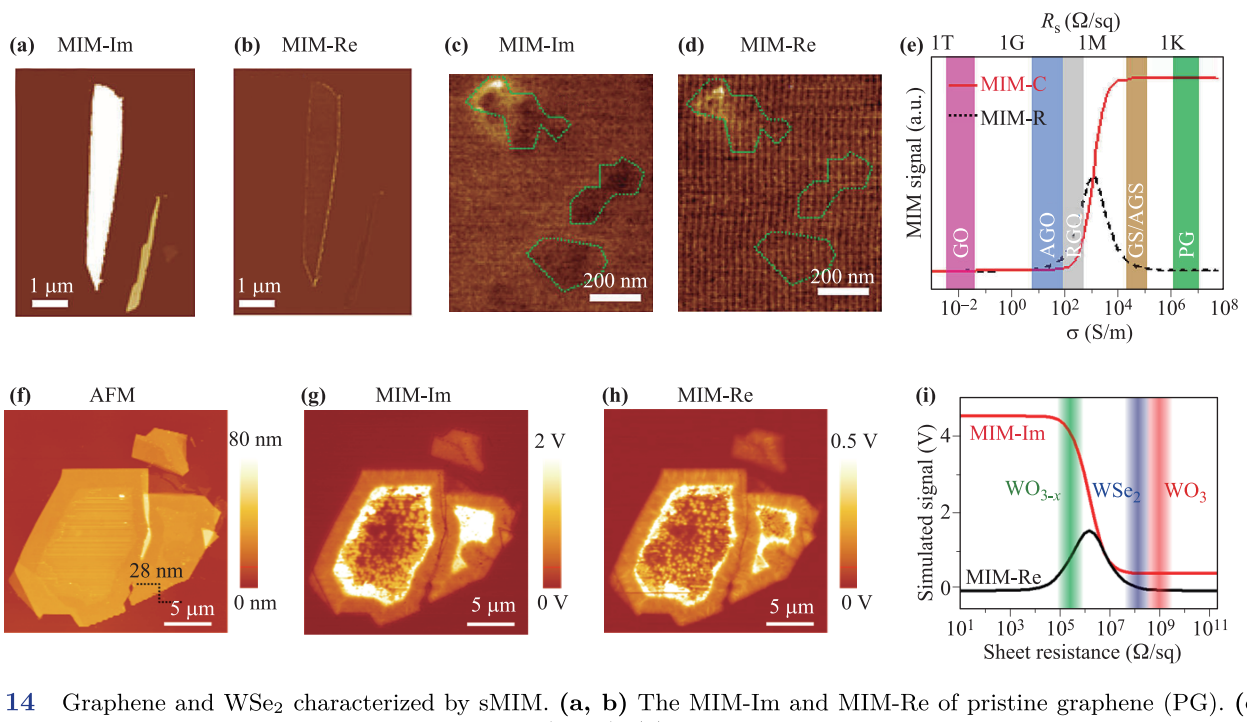


Fig. 14 Graphene and WSe_2 characterized by sMIM. **(a, b)** The MIM-Im and MIM-Re of pristine graphene (PG). **(c, d)** MIM-Im and MIM-Re maps of annealed graphene oxide (AGO). **(e)** Simulated sMIM response as a function of the conductivity of a thin sheet of specimen. It describes the conductivity ranges of chemically derived and pristine graphene in different colors. Reproduced with permission from Ref. [97]. Copyright © 2007 Journal of Nano Letters. **(f–h)** The AFM topography, MIM-Im and MIM-Re images of WSe_2 respectively. The highly conductive regions are brighter in the sMIM maps. **(i)** Simulated MIM-Im and MIM-Re signals as a function of the sheet resistance respectively. Reproduced with permission from Ref. [96]. Copyright © 2015 Journal of Nano Letters.

rials [101, 163]. Lu *et al.* employed PFM to investigate the piezoelectric response which occurs through out-of-plane deformation in CVD grown MoSSe monolayer on highly oriented pyrolytic graphite (HOPG) substrate [81]. In randomized alloy MoSSe monolayer, as shown in Figs. 15(a–c), there is no mechanical/electrochemical contrast. However, Janus MoSSe experimentally shows an intrinsic vertical piezoelectric response, as shown in Figs. 15(d–f). The reason is that, in Janus MoSSe monolayer, the distortion of Mo–S and Mo–Se bonds under an electric field does not cancel, and a net thickness change is induced by applying a vertical voltage. Figure 15(g) illustrates line profiles of both topographic and piezoelectric response along red dashed lines. The different piezoelectric amplitude levels of the Janus MoSSe monolayer and the substrate are also indicated, from which we estimate an out-of-plane d_{33} of Janus MoSSe. The value of d_{33} is calculated as 0.1 pm/V. This is the first demonstration of the vertical piezoelectric response in single-molecular-layer crystal.

Subsequently, Zhou *et al.* used PFM to investigate the out-of-plane piezo and ferroelectric response in α-In_2Se_3 flakes on gold substrate [220]. Figure 15(h) shows the topography of α-In_2Se_3 flakes with the thickness ranging from 3 to 60 nm. Meanwhile, clear out-of-plan domains are demonstrated in PFM images, as shown in Figs. 15(i, j). It is worth noting that some domains wall coincides with the location of the flakes edges, which suggest that PFM phase contrast most likely comes from real polarization contribution rather than other artifacts between different layers. They have also demonstrated that the PFM amplitude and phase hysteresis loops on a 20nm thick In_2Se_3 flakes which are shown in Figs. 15(k) and (l). The amplitude response shows a butterfly loop with an opening of ~1.5 V, whereas the phase switches 180° at the same turning points. Furthermore, the electromechanical response [101, 156] and switching behavior [102] of other 2D materials have also been studied by PFM.

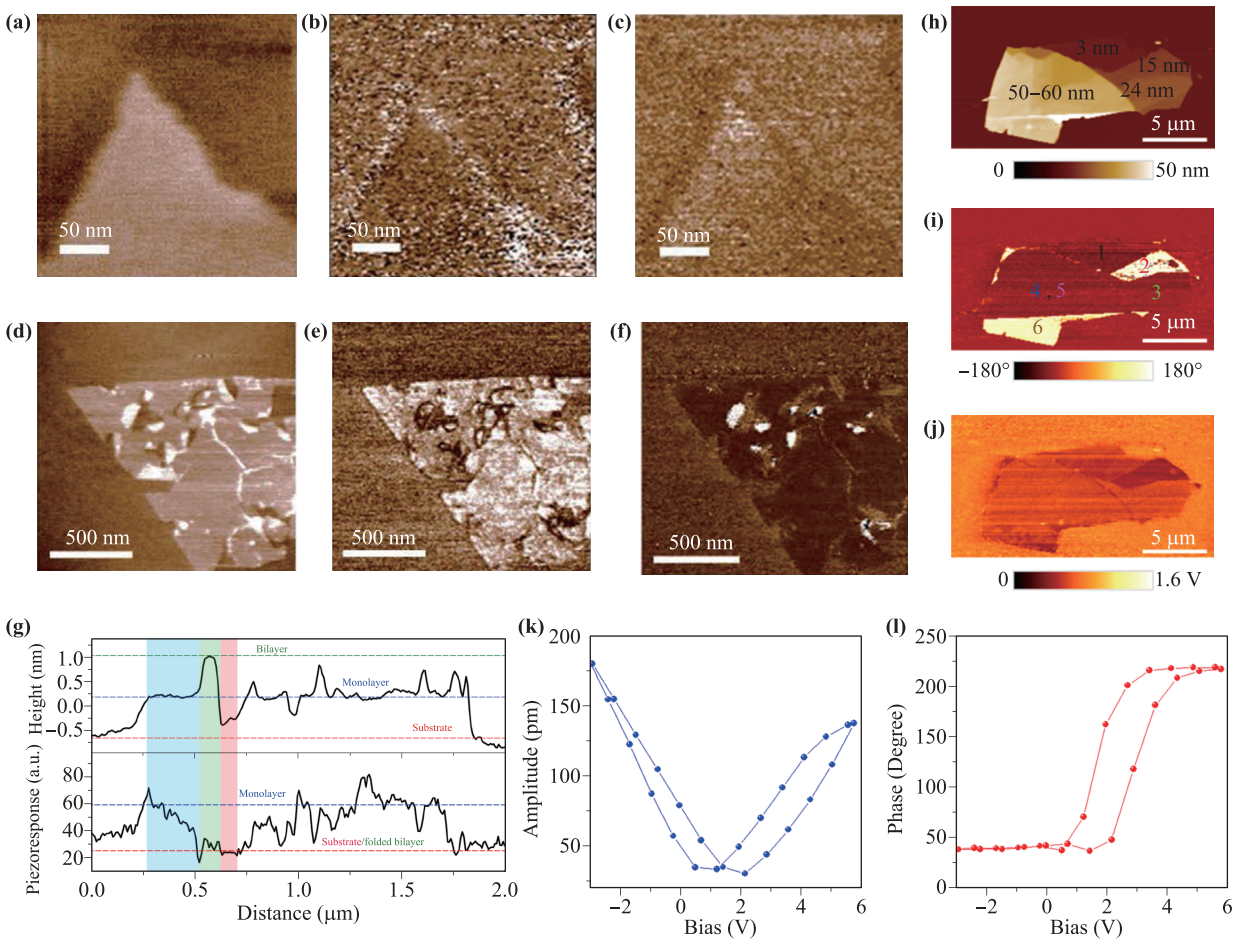


Fig. 15 Electromechanical response characterized by PFM. **(a–c)** Topography, amplitude and phase images of MoSSe alloy sample. The piezoresponse contrast is negligible. **(d–f)** The topography, amplitude and phase images of Janus monolayer MoSSe. The piezoresponse contrast is noteworthy. **(g)** Line profile along in red dashed lines in (d) and (e). Reproduced with permission from Ref. [81]. Copyright © 2017 Journal of Nature Nanotechnology. **(h–j)** AFM, PFM phase and amplitude mapping of mechanical exfoliation α-In_2Se_3 flakes respectively. **(k, l)** PFM amplitude and PFM phase hysteresis loops on a 20 nm thick flake. Reproduced with permission from Ref. [220]. Copyright © 2017 Journal of Nano Letters.

4 Conclusion and perspectives

The electrical properties of two-dimensional materials differ from their bulk counterparts, and further research about their electrical properties at nanoscale is needed. This review highlights the principles of AFM based electrical characterization methods and their further applications in 2D materials. As we have shown, usage of these AFM based electrical characterization methods requires the researchers not only have clear physic concepts, but also are familiar with electronic circuit knowledge. In C-AFM, AFM probe acts as a counter electrode to directly measure the current distribution of sample [221], which is performed in contact mode. KPFM and EFM modes are based on AC mode, which is non-destructive for the sample surface [209]. KPFM can detect the work function of sample, while EFM has the potential to explore the carrier concentration, electrostatic gradient, mobile charge carrier and so on. In SMM, the dielectric constant, doping density, conductivity and permittivity can be obtained (semi-) quantitatively by combining the FEA analysis. In PFM, the piezoelectric coefficient can be measured through detecting the first-harmonic component $A_{1\omega}$.

During the applied research on electrical properties of 2D materials, we found that these AFM modes still need further development and improvement. For example, (i) owing to electrical properties are always coupled with other properties, a method that can explore the mechanical-thermal-electrical-optical coupling is needed. Although PFM and Near-field scanning optical microscopy (SNOM) [219, 222] provide possibility to study the mechanical-electrical and optical-electrical characteristic, we still need to develop advanced technology to achieve multi-field coupling investigation. (ii) It is expected that one can monitor the carrier distribution and electric field distribution of device in work condition. Improving the application of 2D materials and optimizing performance of their devices require the understanding of properties under work condition. A method can detect devices under work condition is crucially required for the future research.

All the above-mentioned AFM techniques provide a key insight in the fields of 2D materials to explore the electrical properties with high-resolution images. With the development of the AFM technology and 2D material preparation, we expect more and more exciting achievements obtained in this field.

Acknowledgements This project was supported by the National Natural Science Foundation of China (NSFC) (Nos. 21622304, 61674045, and 11604063), the Ministry of Science and Technology (MOST) of China (No. 2016YFA0200700), the Strategic Priority Research Program, the Key Research Program of Frontier Sciences and Instrument Developing Project of Chinese Academy of Sciences (CAS) (Nos. XDB30000000, QYZDB-SSW-SYS031, and YZ201418), Osaka University's International Joint Research Promotion Program (Nos. J171013014 and J171013007). Z. H. Cheng was supported by Distinguished Technical Talents Project and Youth Innovation Promotion Association CAS, the Fundamental Research Funds for the Central Universities and the Research Funds of Renmin University of China (No. 18XNLG01).

References

1. H. T. Yuan, H. T. Wang, and Y. Cui, Two-dimensional layered chalcogenides: From rational synthesis to property control via orbital occupation and electron filling, *Acc. Chem. Res.* 48(1), 81 (2015)
2. K. S. Novoselov, A. Mishchenko, A. Carvalho, and A. H. Castro Neto, 2D materials and van der Waals heterostructures, *Science* 353(6298), aac9439 (2016)
3. J. W. May, Platinum surface LEED rings, *Surf. Sci.* 17(1), 267 (1969)
4. K. S. Novoselov, A. K. Geim, S. V. Morozov, D. Jiang, Y. Zhang, S. V. Dubonos, I. V. Grigorieva, and A. A. Firsov, Electric field effect in atomically thin carbon films, *Science* 306(5696), 666 (2004)
5. I. Meric, N. Baklitskaya, P. Kim, and K. L. Shepard, RF performance of top-gated, zero-bandgap graphene field-effect transistors, *2008 International Electron Devices Meeting*, San Francisco, CA, 2008, pp 1–4
6. I. Meric, M. Y. Han, A. F. Young, B. Ozyilmaz, P. Kim, and K. L. Shepard, Current saturation in zero-bandgap, top-gated graphene field-effect transistors, *Nat. Nanotechnol.* 3(11), 654 (2008)
7. M. I. Katsnelson, Graphene: Carbon in two dimensions, *Mater. Today* 10(1–2), 20 (2007)
8. A. A. Balandin, S. Ghosh, W. Z. Bao, I. Calizo, D. Teweldebrhan, F. Miao, and C. N. Lau, Superior thermal conductivity of single-layer graphene, *Nano Lett.* 8(3), 902 (2008)
9. X. Xu, L. F. C. Pereira, Y. Wang, J. Wu, K. Zhang, X. Zhao, S. Bae, C. Tinh Bui, R. Xie, J. T. L. Thong, B. H. Hong, K. P. Loh, D. Donadio, B. Li, and B. Özyilmaz, Length-dependent thermal conductivity in suspended single-layer graphene, *Nat. Commun.* 5(1), 3689 (2014)
10. S. V. Morozov, K. S. Novoselov, M. I. Katsnelson, F. Schedin, D. C. Elias, J. A. Jaszczak, and A. K. Geim, Giant intrinsic carrier mobilities in graphene and its bilayer, *Phys. Rev. Lett.* 100(1), 016602 (2008)
11. M. Han, B. Ozyilmaz, Y. Zhang, P. Jarillo-Herero, and P. Kim, Electronic transport measurements in graphene nanoribbons, *Phys. Status Solidi B* 244(11), 4134 (2007)
12. A. Sikora, M. Woszczyna, M. Friedemann, F. J. Ahlers, and M. Kalbac, AFM diagnostics of graphene-based quantum Hall devices, *Micron* 43(2–3), 479 (2012)
13. C. Zhu, D. Du and Y. Lin, Graphene and graphene-like 2D materials for optical biosensing and bioimaging: A review, *2D Mater.* 2(3), 032004 (2015)

14. M. C. Lemme, T. J. Echtermeyer, M. Baus, and H. Kurz, A graphene field-effect device, *IEEE Electr. Device L*, 28(4), 282 (2007)
15. N. D. Lu, L. F. Wang, L. Li, and M. Liu, A review for compact model of graphene field-effect transistors, *Chin. Phys. B* 26(3), 036804 (2017)
16. F. Bonaccorso, Z. Sun, T. Hasan, and A. C. Ferrari, Graphene photonics and optoelectronics, *Nat. Photonics* 4(9), 611 (2010)
17. Q. L. Bao and K. P. Loh, Graphene photonics, plasmonics, and broadband optoelectronic devices, *ACS Nano* 6(5), 3677 (2012)
18. F. Yavari and N. Koratkar, Graphene-based chemical sensors, *J. Phys. Chem. Lett.* 3(13), 1746 (2012)
19. J. D. Fowler, M. J. Allen, V. C. Tung, Y. Yang, R. B. Kaner, and B. H. Weiller, Practical chemical sensors from chemically derived graphene, *ACS Nano* 3(2), 301 (2009)
20. M. S. Lee, K. Lee, S. Y. Kim, H. Lee, J. Park, K. H. Choi, H. K. Kim, D. G. Kim, D. Y. Lee, S. Nam, and J. U. Park, High-performance, transparent, and stretchable electrodes using graphene–metal nanowire hybrid structures, *Nano Lett.* 13(6), 2814 (2013)
21. I. N. Kholmanov, S. H. Domingues, H. Chou, X. H. Wang, C. Tan, J. Y. Kim, H. F. Li, R. Piner, A. J. G. Zarbin, and R. S. Ruoff, Reduced graphene oxide/copper nanowire hybrid films as high-performance transparent electrodes, *ACS Nano* 7(2), 1811 (2013)
22. X. Miao, S. Tongay, M. K. Petterson, K. Berke, A. G. Rinzler, B. R. Appleton, and A. F. Hebard, High efficiency graphene solar cells by chemical doping, *Nano Lett.* 12(6), 2745 (2012)
23. Z. Liu, J. Li, and F. Yan, Package-free flexible organic solar cells with graphene top electrodes, *Adv. Mater.* 25(31), 4296 (2013)
24. K. S. Novoselov, D. Jiang, F. Schedin, T. J. Booth, V. V. Khotkevich, S. V. Morozov, and A. K. Geim, Two-dimensional atomic crystals, *Proc. Natl. Acad. Sci. USA* 102(30), 10451 (2005)
25. S. Z. Butler, S. M. Hollen, L. Y. Cao, Y. Cui, J. A. Gupta, H. R. Gutierrez, T. F. Heinz, S. S. Hong, J. X. Huang, A. F. Ismach, E. Johnston-Halperin, M. Kuno, V. V. Plashnitsa, R. D. Robinson, R. S. Ruoff, S. Salahuddin, J. Shan, L. Shi, M. G. Spencer, M. Terrones, W. Windl, and J. E. Goldberger, Progress, challenges, and opportunities in two-dimensional materials beyond graphene, *ACS Nano* 7(4), 2898 (2013)
26. Mas-Ballesté, C. Gomez-Navarro, J. Gomez-Herrero, and F. Zamora, 2D materials: To graphene and beyond, *Nanoscale* 3(1), 20 (2011)
27. L. Britnell, R. V. Gorbachev, R. Jalil, B. D. Belle, F. Schedin, A. Mishchenko, T. Georgiou, M. I. Katsnelson, L. Eaves, S. V. Morozov, N. M. R. Peres, J. Leist, A. K. Geim, K. S. Novoselov, and L. A. Ponomarenko, Field-effect tunneling transistor based on vertical graphene heterostructures, *Science* 335(6071), 947 (2012)
28. L. Britnell, R. V. Gorbachev, R. Jalil, B. D. Belle, F. Schedin, M. I. Katsnelson, L. Eaves, S. V. Morozov, A. S. Mayorov, N. M. R. Peres, A. H. Castro Neto, J. Leist, A. K. Geim, L. A. Ponomarenko, and K. S. Novoselov, Electron tunneling through ultrathin boron nitride crystalline barriers, *Nano Lett.* 12(3), 1707 (2012)
29. C. R. Dean, A. F. Young, I. Meric, C. Lee, L. Wang, S. Sorgenfrei, K. Watanabe, T. Taniguchi, P. Kim, K. L. Shepard, and J. Hone, Boron nitride substrates for high-quality graphene electronics, *Nat. Nanotechnol.* 5(10), 722 (2010)
30. R. A. Doganov, E. C. T. O'Farrell, S. P. Koenig, Y. Yeo, A. Ziletti, A. Carvalho, D. K. Campbell, D. F. Coker, K. Watanabe, T. Taniguchi, A. H. C. Neto, and B. Özyilmaz, Transport properties of pristine few-layer black phosphorus by van der Waals passivation in an inert atmosphere, *Nat. Commun.* 6(1), 6647 (2015)
31. Q. H. Wang, K. Kalantar-Zadeh, A. Kis, J. N. Coleman, and M. S. Strano, Electronics and optoelectronics of two-dimensional transition metal dichalcogenides, *Nat. Nanotechnol.* 7(11), 699 (2012)
32. A. Kumar, and P. K. Ahluwalia, Electronic structure of transition metal dichalcogenides monolayers 1H-MX_2 (M = Mo, W; X = S, Se, Te) from ab-initio theory: New direct band gap semiconductors, *Eur. Phys. J. B* 85(6), 186 (2012)
33. B. Radisavljevic, A. Radenovic, J. Brivio, V. Giacometti, and A. Kis, Single-layer MoS_2 transistors, *Nat. Nanotechnol.* 6(3), 147 (2011)
34. A. Splendiani, L. Sun, Y. B. Zhang, T. S. Li, J. Kim, C. Y. Chim, G. Galli, and F. Wang, Emerging photoluminescence in monolayer MoS_2, *Nano Lett.* 10(4), 1271 (2010)
35. S. V. Kalinin and D. A. Bonnell, Imaging mechanism of piezoresponse force microscopy of ferroelectric surfaces, *Phys. Rev. B* 65(12), 125408 (2002)
36. X. Xi, L. Zhao, Z. Wang, H. Berger, L. Forro, J. Shan, and K. F. Mak, Strongly enhanced charge-density-wave order in monolayer $NbSe_2$, *Nat. Nanotechnol.* 10(9), 765 (2015)
37. X. Xi, Z. Wang, W. Zhao, J. H. Park, K. T. Law, H. Berger, L. Forró, J. Shan, and K. F. Mak, Ising pairing in superconducting $NbSe_2$ atomic layers, *Nat. Phys.* 12(2), 139 (2016)
38. A. W. Tsen, B. Hunt, Y. D. Kim, Z. J. Yuan, S. Jia, R. J. Cava, J. Hone, P. Kim, C. R. Dean, and A. N. Pasupathy, Nature of the quantum metal in a two-dimensional crystalline superconductor, *Nat. Phys.* 12(3), 208 (2016)
39. S. J. Kim, K. Choi, B. Lee, Y. Kim, and B. H. Hong, Materials for flexible, stretchable electronics: Graphene and 2D materials, *Annu. Rev. Mater. Res.* 45(1), 63 (2015)
40. J. Pu, Y. Yomogida, K. K. Liu, L. J. Li, Y. Iwasa, and T. Takenobu, Highly flexible MoS_2 thin-film transistors with ion gel dielectrics, *Nano Lett.* 12(8), 4013 (2012)
41. D. Deng, K. S. Novoselov, Q. Fu, N. Zheng, Z. Tian and X. Bao, Catalysis with two-dimensional materials and their heterostructures, *Nat. Nanotechnol.* 11(3), 218 (2016)

42. J. Deng, D. Deng, and X. Bao, Robust catalysis on 2D materials encapsulating metals: Concept, application, and perspective, *Adv. Mater.* 29(43), 1606967 (2017)

43. F. K. Perkins, A. L. Friedman, E. Cobas, P. M. Campbell, G. G. Jernigan, and B. T. Jonker, Chemical vapor sensing with monolayer MoS_2, *Nano Lett.* 13(2), 668 (2013)

44. B. Cho, A. R. Kim, D. J. Kim, H. S. Chung, S. Y. Choi, J. D. Kwon, S. W. Park, Y. Kim, B. H. Lee, K. H. Lee, D. H. Kim, J. Nam, and M. G. Hahm, Two-dimensional atomic-layered alloy junctions for high-performance wearable chemical sensor, *ACS Appl. Mater. Interfaces* 8(30), 19635 (2016)

45. J. Seo, J. Jang, S. Park, C. Kim, B. Park, and J. Cheon, Two-dimensional SnS_2 nanoplates with extraordinary high discharge capacity for lithium ion batteries, *Adv. Mater.* 20(22), 4269 (2008)

46. K. S. Chen, I. Balla, N. S. Luu, and M. C. Hersam, Emerging opportunities for two-dimensional materials in lithium-ion batteries, *ACS Energy Lett.* 2(9), 2026 (2017)

47. N. Perea-López, A. L. Elías, A. Berkdemir, A. Castro-Beltran, H. R. Gutiérrez, S. Feng, R. Lv, T. Hayashi, F. López-Urías, S. Ghosh, B. Muchharla, S. Talapatra, H. Terrones, and M. Terrones, Photosensor device based on few-layered WS_2 films, *Adv. Funct. Mater.* 23(44), 5511 (2013)

48. N. Perea-López, Z. Lin, N. R. Pradhan, A. Iñiguez-Rábago, A. Laura Elías, A. McCreary, J. Lou, P. M. Ajayan, H. Terrones, L. Balicas and M. Terrones, CVD-grown monolayered MoS_2 as an effective photosensor operating at low-voltage, *2D Mater.* 1(1), 011004 (2014)

49. M. Amani, M. L. Chin, A. G. Birdwell, T. P. O'Regan, S. Najmaei, Z. Liu, P. M. Ajayan, J. Lou, and M. Dubey, Electrical performance of monolayer MoS_2 field-effect transistors prepared by chemical vapor deposition, *Appl. Phys. Lett.* 102(19), 193107 (2013)

50. S. Ahmed and J. Yi, Two-dimensional transition metal dichalcogenides and their charge carrier mobilities in field-effect transistors, *Nano-Micro Lett.* 9(4), 50 (2017)

51. G. Binnig, C. F. Quate, and C. Gerber, Atomic force microscope, *Phys. Rev. Lett.* 56(9), 930 (1986)

52. G. Binnig, C. Gerber, E. Stoll, T. R. Albrecht, and C. F. Quate, Atomic resolution with atomic force microscope, *Europhys. Lett.* 3(12), 1281 (1987)

53. Y. Martin, C. C. Williams, and H. K. Wickramasinghe, Atomic force microscope–force mapping and profiling on a sub 100-Å scale, *J. Appl. Phys.* 61(10), 4723 (1987)

54. M. Nonnenmacher, M. P. Oboyle, and H. K. Wickramasinghe, Kelvin probe force microscopy, *Appl. Phys. Lett.* 58(25), 2921 (1991)

55. F. Pérez-Murano, G. Abadal, N. Barniol, X. Aymerich, J. Servat, P. Gorostiza, and F. Sanz, Nanometer-scale oxidation of Si(100) surfaces by tapping mode atomic force microscopy, *J. Appl. Phys.* 78(11), 6797 (1995)

56. R. García and R. Perez, Dynamic atomic force microscopy methods, *Surf. Sci. Rep.* 47(6–8), 197 (2002)

57. H. Hölscher and U. D. Schwarz, Theory of amplitude modulation atomic force microscopy with and without Q-control, *Int. J. Non-linear Mech.* 42(4), 608 (2007)

58. Y. Sugawara, T. Uchihashi, M. Abe, and S. Morita, True atomic resolution imaging of surface structure and surface charge on the GaAs(110), *Appl. Surf. Sci.* 140(3–4), 371 (1999)

59. S. K. Jang, J. Youn, Y. J. Song, and S. Lee, Synthesis and characterization of hexagonal boron nitride as a gate dielectric, *Sci. Rep.* 6(1), 30449 (2016)

60. A. Belianinov, S. V. Kalinin, and S. Jesse, Complete information acquisition in dynamic force microscopy, *Nat. Commun.* 6(1), 6550 (2015)

61. H. Martinez, C. Auriel, D. Gonbeau, M. Loudet, and G. Pfister-Guillouzo, Studies of 1T TiS_2 by STM, AFM and XPS: The mechanism of hydrolysis in air, *Appl. Surf. Sci.* 93(3), 231 (1996)

62. M. G. Ruppert, D. M. Harcombe, M. R. P. Ragazzon, S. O. R. Moheimani, and A. J. Fleming, A review of demodulation techniques for amplitude-modulation atomic force microscopy, *Beilstein J. Nanotechnol.* 8, 1407 (2017)

63. Z. Zheng, R. Xu, S. Ye, S. Hussain, W. Ji, P. Cheng, Y. Li, Y. Sugawara, and Z. Cheng, High harmonic exploring on different materials in dynamic atomic force microscopy, *Sci. China Tech. Sci.* 61(3), 446 (2018)

64. G. Benstetter, R. Biberger, and D. P. Liu, A review of advanced scanning probe microscope analysis of functional films and semiconductor devices, *Thin Solid Films* 517(17), 5100 (2009)

65. R. A. Oliver, Advances in AFM for the electrical characterization of semiconductors, *Rep. Prog. Phys.* 71(7), 076501 (2008)

66. A. Avila and B. Bhushan, Electrical measurement techniques in atomic force microscopy, *Crit. Rev. Solid State Mater. Sci.* 35(1), 38 (2010)

67. S. Liu and Y. Wang, A review of the application of atomic force microscopy (AFM) in food science and technology, *Adv. Food Nutr. Res.* 62, 201 (2011)

68. I. Pecorari, L. Puzzi, and O. Sbaizero, Atomic force microscopy and lamins: A review study towards future, combined investigations, *Microsc. Res. Tech.* 80(1), 97 (2017)

69. S. V. Kontomaris and A. Stylianou, Atomic force microscopy for university students: Applications in biomaterials, *Eur. J. Phys.* 38(3), 033003 (2017)

70. M. Li, D. Dang, L. Q. Liu, N. Xi, and Y. C. Wang, Atomic force microscopy in characterizing cell mechanics for biomedical applications: A review, *IEEE. T. Nanobiosci.* 16(6), 523 (2017)

71. F. Houzé, R. Meyer, O. Schneegans, and L. Boyer, Imaging the local electrical properties of metal surfaces by atomic force microscopy with conducting probes, *Appl. Phys. Lett.* 69(13), 1975 (1996)

72. J. E. Shaw, A. Perumal, D. D. C. Bradley, P. N. Stavrinou, and T. D. Anthopoulos, Nanoscale current spreading analysis in solution-processed graphene oxide/silver nanowire transparent electrodes via conductive atomic force microscopy, *J. Appl. Phys.* 119(19), 195501 (2016)

73. F. Giannazzo, G. Fisichella, A. Piazza, S. Di Franco, I. P. Oliveri, S. Agnello, and F. Roccaforte, Current injection from metal to MoS_2 probed at nanoscale by conductive atomic force microscopy, *Mater. Sci. Semicond. Process.* 42, 174 (2016)
74. J. Yang, P. Gordiichuk, O. Zheliuk, J. Lu, A. Herrmann, and J. Ye, Role of defects in tuning the electronic properties of monolayer WS_2 grown by chemical vapor deposition, *Phys. Status Solidi RRL.* 11(10), 1700302 (2017)
75. M. R. Rosenberger, H. J. Chuang, K. M. McCreary, C. H. Li, and B. T. Jonker, Electrical characterization of discrete defects and impact of defect density on photoluminescence in monolayer WS_2, *ACS Nano* 12(2), 1793 (2018)
76. S. J. O'Shea, Conducting atomic force microscopy study of silicon dioxide breakdown, *J. Vac. Sci. Technol. B* 13(5), 1945 (1995)
77. L. Zhang and Y. Mitani, Structural and electrical evolution of gate dielectric breakdown observed by conductive atomic force microscopy, *Appl. Phys. Lett.* 88(3), 032906 (2006)
78. E. Koren, Y. Rosenwaks, J. E. Allen, E. R. Hemesath, and L. J. Lauhon, Nonuniform doping distribution along silicon nanowires measured by Kelvin probe force microscopy and scanning photocurrent microscopy, *Appl. Phys. Lett.* 95(9), 092105 (2009)
79. H. J. Lee and S. M. Park, Electrochemistry of conductive polymers. 30. Nanoscale measurements of doping distributions and current-voltage characteristics of electrochemically deposited polypyrrole films, *J. Phys. Chem. B* 108(5), 1590 (2004)
80. R. Vidyasagar, B. Camargo, K. Romanyuk, and A. L. Kholkin, Surface potential distribution of multilayer graphene using Kelvin probe and electric-field force microscopies, *Ferroelectr.* 508(1), 115 (2017)
81. A. Y. Lu, H. Zhu, J. Xiao, C. P. Chuu, Y. Han, M. H. Chiu, C. C. Cheng, C. W. Yang, K. H. Wei, Y. Yang, Y. Wang, D. Sokaras, D. Nordlund, P. Yang, D. A. Muller, M. Y. Chou, X. Zhang, and L. J. Li, Janus monolayers of transition metal dichalcogenides, *Nat. Nanotechnol.* 12(8), 744 (2017)
82. V. Kaushik, D. Varandani, and B. R. Mehta, Nanoscale mapping of layer-dependent surface potential and junction properties of cvd-grown MoS_2 domains, *J. Phys. Chem. C* 119(34), 20136 (2015)
83. T. Filleter, K. V. Emtsev, T. Seyller, and R. Bennewitz, Local work function measurements of epitaxial graphene, *Appl. Phys. Lett.* 93(13), 133117 (2008)
84. Y. Shen, X. Zhang, Y. Wang, X. Zhou, J. Hu, S. Guo, and Y. Zhang, Charge transfer between reduced graphene oxide sheets on insulating substrates, *Appl. Phys. Lett.* 103(5), 053107 (2013)
85. A. Liscio, G. P. Veronese, E. Treossi, F. Suriano, F. Rossella, V. Bellani, R. Rizzoli, P. Samorì, and V. Palermo, Charge transport in graphene–polythiophene blends as studied by Kelvin probe force microscopy and transistor characterization, *J. Mater. Chem.* 21(9), 2924 (2011)
86. L. Yan, C. Punckt, I. A. Aksay, W. Mertin, and G. Bacher, Local voltage drop in a single functionalized graphene sheet characterized by Kelvin probe force microscopy, *Nano Lett.* 11(9), 3543 (2011)
87. M. Lucchesi, G. Privitera, M. Labardi, D. Prevosto, S. Capaccioli, and P. Pingue, Electrostatic force microscopy and potentiometry of realistic nanostructured systems, *J. Appl. Phys.* 105(5), 054301 (2009)
88. S. S. Datta, D. R. Strachan, E. J. Mele, and A. T. C. Johnson, Surface potentials and layer charge distributions in few-layer graphene films, *Nano Lett.* 9(1), 7 (2009)
89. C. K. Oliveira, M. J. S. Matos, M. S. C. Mazzoni, H. Chacham, and B. R. A. Neves, Anomalous response of supported few-layer hexagonal boron nitride to DC electric fields: A confined water effect? *Nanotechnol.* 23(17), 175703 (2012)
90. L. Collins, J. I. Kilpatrick, S. A. L. Weber, A. Tselev, I. V. Vlassiouk, I. N. Ivanov, S. Jesse, S. V. Kalinin and B. J. Rodriguez, Open loop Kelvin probe force microscopy with single and multi-frequency excitation, *Nanotechnol.* 24(47), 475702 (2013)
91. C. Li, X. D. Ding, and G. C. Lin, Study on multi-frequency method for electrostatic force microscopy in air, *Integr. Ferroelectr.* 145(1), 59 (2013)
92. Y. P. Jiang, Q. Qi, R. Wang, J. Zhang, Q. K. Xue, C. Wang, C. Jiang, and X. H. Qiu, Direct observation and measurement of mobile charge carriers in a monolayer organic semiconductor on a dielectric substrate, *ACS Nano* 5(8), 6195 (2011)
93. C. Gao, T. Wei, F. Duewer, Y. Lu, and X. D. Xiang, High spatial resolution quantitative microwave impedance microscopy by a scanning tip microwave near-field microscope, *Appl. Phys. Lett.* 71(13), 1872 (1997)
94. D. Wu, A. J. Pak, Y. Liu, Y. Zhou, X. Wu, Y. Zhu, M. Lin, Y. Han, Y. Ren, H. Peng, Y. H. Tsai, G. S. Hwang, and K. Lai, Thickness-dependent dielectric constant of few-layer In_2Se_3 nanoflakes, *Nano Lett.* 15(12), 8136 (2015)
95. Y. Feng, K. Zhang, F. Wang, Z. Liu, M. Fang, R. Cao, Y. Miao, Z. Yang, W. Mi, Y. Han, Z. Song, and H. S. Wong, Synthesis of large-area highly crystalline monolayer molybdenum disulfide with tunable grain size in a H_2 atmosphere, *ACS Appl. Mater. Interfaces* 7(40), 22587 (2015)
96. Y. Liu, C. Tan, H. Chou, A. Nayak, D. Wu, R. Ghosh, H. Y. Chang, Y. Hao, X. Wang, J. S. Kim, R. Piner, R. S. Ruoff, D. Akinwande, and K. Lai, Thermal oxidation of WSe_2 nanosheets adhered on SiO_2/Si substrates, *Nano Lett.* 15(8), 4979 (2015)
97. W. Kundhikanjana, K. Lai, H. Wang, H. Dai, M. A. Kelly, and Z. Shen, Hierarchy of electronic properties of chemically derived and pristine graphene probed by microwave imaging, *Nano Lett.* 9(11), 3762 (2009)
98. S. Berweger, P. T. Blanchard, M. D. Brubaker, K. J. Coakley, N. A. Sanford, T. M. Wallis, K. A. Bertness, and P. Kabos, Near-field control and imaging of free charge carrier variations in GaN nanowires, *Appl. Phys. Lett.* 108(7), 073101 (2016)

99. E. Brinciotti, G. Gramse, S. Hommel, T. Schweinboeck, A. Altes, M. A. Fenner, J. Smoliner, M. Kasper, G. Badino, S. S. Tuca, and F. Kienberger, Probing resistivity and doping concentration of semiconductors at the nanoscale using scanning microwave microscopy, *Nanoscale* 7(35), 14715 (2015)
100. H. P. Huber, I. Humer, M. Hochleitner, M. Fenner, M. Moertelmaier, C. Rankl, A. Imtiaz, T. M. Wallis, H. Tanbakuchi, P. Hinterdorfer, P. Kabos, J. Smoliner, J. J. Kopanski, and F. Kienberger, Calibrated nanoscale dopant profiling using a scanning microwave microscope, *J. Appl. Phys.* 111(1), 014301 (2012)
101. S. K. Kim, R. Bhatia, T. H. Kim, D. Seol, J. H. Kim, H. Kim, W. Seung, Y. Kim, Y. H. Lee, and S. W. Kim, Directional dependent piezoelectric effect in CVD grown monolayer MoS_2 for flexible piezoelectric nanogenerators, *Nano Energy* 22, 483 (2016)
102. M. Park, S. Hong, J. Kim, J. Hong, and K. No, Nanoscale ferroelectric switching behavior at charged domain boundaries studied by angle-resolved Piezoresponse force microscopy, *Appl. Phys. Lett.* 99(14), 142909 (2011)
103. S. Kim, V. Gopalan, and A. Gruverman, Coercive fields in ferroelectrics: A case study in lithium niobate and lithium tantalate, *Appl. Phys. Lett.* 80(15), 2740 (2002)
104. R. Xu, L. J. Yin, J. B. Qiao, K. K. Bai, J. C. Nie, and L. He, Direct probing of the stacking order and electronic spectrum of rhombohedral trilayer graphene with scanning tunneling microscopy, *Phys. Rev. B* 91(3), 035410 (2015)
105. C. J. Chen, Introduction to Scanning Tunneling Microscopy, Columbia University, 2008
106. M. P. Murrell, M. E. Welland, S. J. O'Shea, T. M. H. Wong, J. R. Barnes, A. W. McKinnon, M. Heyns, and S. Verhaverbeke, Spatially resolved electrical measurements of SiO_2 gate oxides using atomic force microscopy, *Appl. Phys. Lett.* 62(7), 786 (1993)
107. A. A. Pomarico, D. Huang, J. Dickinson, A. A. Baski, R. Cingolani, H. Morkoc, and R. Molnar, Current mapping of GaN films by conductive atomic force microscopy, *Appl. Phys. Lett.* 82(12), 1890 (2003)
108. W. Frammelsberger, G. Benstetter, J. Kiely, and R. Stamp, C-AFM-based thickness determination of thin and ultra-thin SiO2 films by use of different conductive-coated probe tips, *Appl. Surf. Sci.* 253(7), 3615 (2007)
109. P. De Wolf, T. Clarysse, and W. Vandervorst, Quantification of nanospreading resistance profiling data, *J. Vac. Sci. Technol. B* 16(1), 320 (1998)
110. J. M. Mativetsky, Y. L. Loo, and P. Samorì, Elucidating the nanoscale origins of organic electronic function by conductive atomic force microscopy, *J. Mater. Chem. C Mater. Opt. Electron. Devices* 2(17), 3118 (2014)
111. H. O. Jacobs, P. Leuchtmann, O. J. Homan, and A. Stemmer, Resolution and contrast in Kelvin probe force microscopy, *J. Appl. Phys.* 84(3), 1168 (1998)
112. J. W. P. Hsu, H. M. Ng, A. M. Sergent, and S. N. G. Chu, Scanning Kelvin force microscopy imaging of surface potential variations near threading dislocations in GaN, *Appl. Phys. Lett.* 81(19), 3579 (2002)
113. J. Ren, H. D. Liess, R. Mackel, and H. Baumgartner, Scanning kelvin microscope: A new method for surface investigations, *Fresenius J. Anal. Chem.* 353(3–4), 303 (1995)
114. L. Collins, S. Jesse, N. Balke, B. J. Rodriguez, S. Kalinin, and Q. Li, Band excitation Kelvin probe force microscopy utilizing photothermal excitation, *Appl. Phys. Lett.* 106(10), 104102 (2015)
115. S. Guo, S. V. Kalinin, and S. Jesse, Open-loop band excitation Kelvin probe force microscopy, *Nanotechnol.* 23(12), 125704 (2012)
116. M. Neek-Amal, L. Covaci, K. Shakouri, and F. Peeters, Electronic structure of a hexagonal graphene flake subjected to triaxial stress, *Phys. Rev. B* 88(11), 115428 (2013)
117. P. De Wolf, R. Stephenson, T. Trenkler, T. Clarysse, T. Hantschel, and W. Vandervorst., Status and review of two-dimensional carrier and dopant profiling using scanning probe microscopy, *J. Vac. Sci. Technol. B* 18(1), 361 (2000)
118. W. Melitz, J. Shen, A. C. Kummel, and S. Lee, Kelvin probe force microscopy and its application, *Surf. Sci. Rep.* 66(1), 1 (2011)
119. B. Bhushan and A. V. Goldade, Kelvin probe microscopy measurements of surface potential change under wear at low loads, *Wear* 244(1–2), 104 (2000)
120. L. Tetard, A. Passian, and T. Thundat, New modes for subsurface atomic force microscopy through nanomechanical coupling, *Nat. Nanotechnol.* 5(2), 105 (2010)
121. R. W. Stark, N. Naujoks, and A. Stemmer, Multifrequency electrostatic force microscopy in the repulsive regime, *Nanotechnol.* 18(6), 065502 (2007)
122. X. D. Ding, J. An, J. B. Xu, C. Li, and R. Y. Zeng, Improving lateral resolution of electrostatic force microscopy by multifrequency method under ambient conditions, *Appl. Phys. Lett.* 94(22), 223109 (2009)
123. T. R. Albrecht, P. Grütter, D. Horne, and D. Rugar, Frequency modulation detection using high-Q cantilevers for enhanced force microscope sensitivity, *J. Appl. Phys.* 69(2), 668 (1991)
124. L. Fumagalli, M. A. Edwards, and G. Gomila, Quantitative electrostatic force microscopy with sharp silicon tips, *Nanotechnol.* 25(49), 495701 (2014)
125. S. Gómez-Moñivas, L. S. Froufe, R. Carminati, J. J. Greffet, and J. J. Saenz, Tip-shape effects on electrostatic force microscopy resolution, *Nanotechnol.* 12(4), 496 (2001)
126. C. Schönenberger and S. F. Alvarado, Observation of single charge carriers by force microscopy, *Phys. Rev. Lett.* 65(25), 3162 (1990)
127. C. Schönenberger, Charge flow during metal-insulator contact, *Phys. Rev. B* 45, 3861 (1992)
128. S. Gómez-Moñivas, L. S. Froufe-Pérez, A. J. Caamaño, and J. J. Sáenz, Electrostatic forces between sharp tips and metallic and dielectric samples, *Appl. Phys. Lett.* 79(24), 4048 (2001)

129. K. Zhang, N. Marzari, and Q. Zhang, Covalently functionalized metallic single-walled carbon nanotubes studied using electrostatic force microscopy and dielectric force microscopy, *J. Phys. Chem. C* 117(46), 24570 (2013)

130. S. C. Jr Fain, K. A. Barry, M. G. Bush, B. Pittenger, and R. N. Louie, Measuring average tip-sample forces in intermittent-contact (tapping) force microscopy in air, *Appl. Phys. Lett.* 76, 930 (2000)

131. C. Riedel, G. A. Schwartz, R. Arinero, P. Tordjeman, G. Leveque, A. Alegria, and J. Colmenero, Nanoscale dielectric properties of insulating thin films: From single point measurements to quantitative images, *Ultramicroscopy* 110(6), 634 (2010)

132. P. Girard, Electrostatic force microscopy: Principles and some applications to semiconductors, *Nanotechnol.* 12(4), 485 (2001)

133. C. Riedel, R. Arinero, P. Tordjeman, M. Ramonda, G. Lévêque, G. A. Schwartz, D. G. Oteyza, A. Alegria, and J. Colmenero, Determination of the nanoscale dielectric constant by means of a double pass method using electrostatic force microscopy, *J. Appl. Phys.* 106(2), 024315 (2009)

134. L. Collins, J. I. Kilpatrick, I. V. Vlassiouk, A. Tselev, S. A. L. Weber, S. Jesse, S. V. Kalinin, and B. J. Rodriguez, Dual harmonic Kelvin probe force microscopy at the graphene–liquid interface, *Appl. Phys. Lett.* 104(13), 133103 (2014)

135. L. Lei, R. Xu, S. Ye, X. Wang, K. Xu, S. Hussain, Y. Li, Y. Sugawara, L. Xie, W. Ji, and Z. Cheng, Local characterization of mobile charge carriers by two electrical AFM modes: Multi-harmonic EFM versus sMIM, *J. Phys. Commun.* 2(2), 025013 (2018)

136. J. P. Colinge and C. A. Colinge, Physics of Semiconductor, University of California, 2005

137. B. D. Terris, J. E. Stern, D. Rugar, and H. J. Mamin, Localized charge force microscopy, *J. Vac. Sci. Technol. A* 8(1), 374 (1990)

138. Y. Martin, D. W. Abraham, and H. K. Wickramasinghe, High-resolution capacitance measurement and potentiometry by force microscopy, *Appl. Phys. Lett.* 52(13), 1103 (1988)

139. K. Lai, W. Kundhikanjana, M. Kelly, and Z. X. Shen, Modeling and characterization of a cantilever-based near-field scanning microwave impedance microscope, *Rev. Sci. Instrum.* 79(6), 063703 (2008)

140. K. Lai, M. B. Ji, N. Leindecker, M. A. Kelly, and Z. X. Shen, Atomic-force-microscope-compatible near-field scanning microwave microscope with separated excitation and sensing probes, *Rev. Sci. Instrum.* 78(6), 063702 (2007)

141. Y. Tsai, Z. Chu, Y. Han, C. P. Chuu, D. Wu, A. Johnson, F. Cheng, M. Y. Chou, D. A. Muller, X. Li, K. Lai, and C. K. Shih, Tailoring semiconductor lateral multijunctions for giant photoconductivity enhancement, *Adv. Mater.* 29(41), 1703680 (2017)

142. D. Wu, X. Li, L. Luan, X. Y. Wu, W. Li, M. N. Yogeesh, R. Ghosh, Z. D. Chu, D. Akinwande, Q. Niu, and K. Lai, Uncovering edge states and electrical inhomogeneity in MoS_2 field-effect transistors, *Proc. Natl. Acad. Sci. USA* 113(31), 8583 (2016)

143. X. Rui, Z. Zhiyue, J. Wei, and C. Zhihai, Advance scanning microwave microscopy, *Prog. Phys.* 35(6), 241 (2015)

144. K. Lai, W. Kundhikanjana, M. A. Kelly, and Z. X. Shen, Nanoscale microwave microscopy using shielded cantilever probes, *Appl. Nanosci.* 1(1), 13 (2011)

145. Y. Yang, K. Lai, Q. Tang, W. Kundhikanjana, M. A. Kelly, K. Zhang, Z. Shen, and X. Li, Batch-fabricated cantilever probes with electrical shielding for nanoscale dielectric and conductivity imaging, *J. Micromech. Microeng.* 22(11), 115040 (2012)

146. G. Agustí, S. Cobo, A. B. Gaspar, G. Molnár, N. O. Moussa, P. Á. Szilágyi, V. Pálfi, C. Vieu, M. C. Munoz, J. A. Real, and A. Bousseksou, Thermal and light-induced spin crossover phenomena in new 3D Hofmann-like microporous metalorganic frameworks produced as bulk materials and nanopatterned thin films, *Chem. Mater.* 20(21), 6721 (2008)

147. A. Tselev, N. V. Lavrik, I. Vlassiouk, D. P. Briggs, M. Rutgers, R. Proksch, and S. V. Kalinin, Near-field microwave scanning probe imaging of conductivity inhomogeneities in CVD graphene, *Nanotechnol.* 23(38), 385706 (2012)

148. H. Madan, M. Jerry, A. Pogrebnyakov, T. Mayer, and S. Datta, quantitative mapping of phase coexistence in Mott-Peierls insulator during electronic and thermally driven phase transition, *ACS Nano* 9(2), 2009 (2015)

149. G. Gramse, M. Kasper, L. Fumagalli, G. Gomila, P. Hinterdorfer and F. Kienberger, Calibrated complex impedance and permittivity measurements with scanning microwave microscopy, *Nanotechnol.* 25(14), 145703 (2014)

150. T. Dargent, K. Haddadi, T. Lasri, N. Clement, D. Ducatteau, B. Legrand, H. Tanbakuchi, and D. Theron, An interferometric scanning microwave microscope and calibration method for sub-fF microwave measurements, *Rev. Sci. Instrum.* 84(12), 123705 (2013)

151. H. P. Huber, M. Moertelmaier, T. M. Wallis, C. J. Chiang, M. Hochleitner, A. Imtiaz, Y. J. Oh, K. Schilcher, M. Dieudonne, J. Smoliner, P. Hinterdorfer, S. J. Rosner, H. Tanbakuchi, P. Kabos, and F. Kienberger, Calibrated nanoscale capacitance measurements using a scanning microwave microscope, *Rev. Sci. Instrum.* 81(11), 113701 (2010)

152. S. Dunn, Determination of cross sectional variation of ferroelectric properties for thin film (Ca. 500 nm) PZT (30/70) via PFM, *Integr. Ferroelectr.* 59(1), 1505 (2003)

153. M. S. Ivanov, N. E. Sherstyuk, E. D. Mishina, V. A. Khomchenko, A. Tselev, V. M. Mukhortov, J. A. Paixão, and A. L. Kholkin, Enhancement of local piezoelectric properties of a perforated ferroelectric thin film visualized via piezoresponse force microscopy, *J. Phys. D* 50(42), 425303 (2017)

154. S. Dunn, C. P. Shaw, Z. Huang, and R. W. Whatmore, Ultrahigh resolution of lead zirconate titanate 30/70 domains as imaged by piezoforce microscopy, *Nanotechnol.* 13(4), 456 (2002)

155. P. Güthner, and K. Dransfeld, Local poling of ferroelectric polymers by scanning force microscopy, *Appl. Phys. Lett.* 61(9), 1137 (1992)

156. Z. Jiang, G. Zheng, K. Zhan, Z. Han, and H. Wang, Mechanisms of polarization switching in graphene oxides and poly (vinylidene fluoride)–graphene oxide films, *Jpn. J. Appl. Phys.* 55(4S), 04EP04 (2016)

157. D. Seol, B. Kim, and Y. Kim, Non-piezoelectric effects in piezoresponse force microscopy, *Curr. Appl. Phys.* 17(5), 661 (2017)

158. F. Li, J. Qi, M. Xu, J. Xiao, Y. Xu, X. Zhang, S. Liu, and Y. Zhang, Layer dependence and light tuning surface potential of 2D MoS_2 on various substrates, *Small* 13(14), 1603103 (2017)

159. E. Soergel, Piezoresponse force microscopy (PFM), *J. Phys. D* 44(46), 464003 (2011)

160. N. A. Burnham, X. Chen, C. S. Hodges, G. A. Matei, E. J. Thoreson, C. J. Roberts, M. C. Davies, and S. J. B. Tendler, Comparison of calibration methods for atomic-force microscopy cantilevers, *Nanotechnol.* 14(1), 1 (2003)

161. S. Hong, H. Shin, J. Woo, and K. No, Effect of cantilever–sample interaction on piezoelectric force microscopy, *Appl. Phys. Lett.* 80(8), 1453 (2002)

162. J. A. Christman, R. R. Jr Woolcott, A. I. Kingon, and R. J. Nemanich, Piezoelectric measurements with atomic force microscopy, *Appl. Phys. Lett.* 73(26), 3851 (1998)

163. C. J. Brennan, R. Ghosh, K. Koul, S. K. Banerjee, N. Lu, and E. T. Yu, Out-of-plane electromechanical response of monolayer molybdenum disulfide measured by Piezoresponse force microscopy, *Nano Lett.* 17(9), 5464 (2017)

164. S. V. Kalinin and D. A. Bonnell, Local potential and polarization screening on ferroelectric surfaces, *Phys. Rev. B* 63(12), 125411 (2001)

165. S. V. Kalinin, D. A. Bonnell, T. Alvarez, X. J. Lei, Z. H. Hu, R. Shao, and J. H. Ferris, Ferroelectric Lithography of Multicomponent Nanostructures, *Adv. Mater.* 16(910), 795 (2004)

166. K. Franke, H. Huelz, and M. Weihnacht, How to extract spontaneous polarization information from experimental data in electric force microscopy, *Surf. Sci.* 415(1–2), 178 (1998)

167. I. Szafraniak, C. Harnagea, R. Scholz, S. Bhattacharyya, D. Hesse, and M. Alexe, Ferroelectric epitaxial nanocrystals obtained by a self-patterning method, *Appl. Phys. Lett.* 83(11), 2211 (2003)

168. J. M. Mativetsky, E. Treossi, E. Orgiu, M. Melucci, G. P. Veronese, P. Samori, and V. Palermo, local current mapping and patterning of reduced graphene oxide, *J. Am. Chem. Soc.* 132(40), 14130 (2010)

169. G. H. Lee, Y. J. Yu, C. Lee, C. Dean, K. L. Shepard, P. Kim, and J. Hone, Electron tunneling through atomically flat and ultrathin hexagonal boron nitride, *Appl. Phys. Lett.* 99(24), 243114 (2011)

170. L. Jiang, Y. Shi, F. Hui, K. Tang, Q. Wu, C. Pan, X. Jing, H. Uppal, F. Palumbo, G. Lu, T. Wu, H. Wang, M. A. Villena, X. Xie, P. C. McIntyre, and M. Lanza, Dielectric breakdown in chemical vapor deposited hexagonal boron nitride, *ACS Appl. Mater. Interfaces* 9(45), 39758 (2017)

171. Y. Hattori, T. Taniguchi, K. Watanabe, and K. Nagashio, Layer-by-layer dielectric breakdown of hexagonal boron nitride, *ACS Nano* 9(1), 916 (2015)

172. Y. Kobayashi, S. Yoshida, R. Sakurada, K. Takashima, T. Yamamoto, T. Saito, S. Konabe, T. Taniguchi, K. Watanabe, Y. Maniwa, O. Takeuchi, H. Shigekawa, and Y. Miyata, Modulation of electrical potential and conductivity in an atomic-layer semiconductor heterojunction, *Sci. Rep.* 6(1), 31223 (2016)

173. H. Lee, N. Son, H. Y. Jeong, T. G. Kim, G. S. Bang, J. Y. Kim, G. W. Shim, K. C. Goddeti, J. H. Kim, N. Kim, H. J. Shin, W. Kim, S. Kim, S. Y. Choi, and J. Y. Park, Friction and conductance imaging of sp^2- and sp^3-hybridized subdomains on single-layer graphene oxide, *Nanoscale* 8, 4063 (2016)

174. D. Ruzmetov, K. H. Zhang, G. Stan, B. Kalanyan, G. R. Bhimanapati, S. M. Eichfeld, R. A. Burke, P. B. Shah, T. P. O'Regan, F. J. Crowne, A. G. Birdwell, J. A. Robinson, A. V. Davydov, and T. G. Ivanov, Vertical 2D/3D semiconductor heterostructures based on epitaxial molybdenum disulfide and gallium nitride, *ACS Nano* 10(3), 3580 (2016)

175. C. S. Pathak, M. Garg, J. P. Singh, and R. Singh, Current transport properties of monolayer graphene/n-Si Schottky diodes, *Semicond. Sci. Technol.* 33(5), 055006 (2018)

176. J. Choi, H. Y. Zhang, H. D. Du, and J. H. Choi, understanding solvent effects on the properties of two-dimensional transition metal dichalcogenides, *ACS Appl. Mater. Interfaces* 8(14), 8864 (2016)

177. S. Choi, Z. Shaolin, and W. Yang, Layer-number-dependent work function of MoS_2 nanoflakes, *J. Korean Phys. Soc.* 64(10), 1550 (2014)

178. K. Chen, X. Wan, J. Wen, W. Xie, Z. Kang, X. Zeng, H. Chen, and J. B. Xu, Electronic properties of MoS_2–WS_2 heterostructures synthesized with two-step lateral epitaxial strategy, *ACS Nano* 9(10), 9868 (2015)

179. F. C. Salomão, E. M. Lanzoni, C. A. Costa, C. Deneke, and E. B. Barros, Determination of high-frequency dielectric constant and surface potential of graphene oxide and influence of humidity by Kelvin probe force microscopy, *Langmuir* 31(41), 11339 (2015)

180. O. Ochedowski, K. Marinov, N. Scheuschner, A. Poloczek, B. K. Bussmann, J. Maultzsch, and M. Schleberger, Effect of contaminations and surface preparation on the work function of single layer MoS_2, *Beilstein J. Nanotechnol.* 5, 291 (2015)

181. Y. Li, C. Y. Xu, J. Y. Wang, and L. Zhen, Photodiode-like behavior and excellent photoresponse of vertical Si/monolayer MoS_2 heterostructures, *Sci. Rep.* 4(1), 7186 (2014)

182. C. B. Jacobs, K. Wang, A. V. Ievlev, L. Collins, E. S. Muckley, and I. N. Ivanov, Functional two/three-dimensional assembly of monolayer WS_2 and nickel oxide, *J. Photonics Energy* 7(1), 014001 (2017)

183. B. J. Robinson, C. E. Giusca, Y. T. Gonzalez, N. D. Kay, O. Kazakova and O. V. Kolosov, Structural, optical and electrostatic properties of single and few-layers MoS_2: effect of substrate, *2D Mater.* 2(1), 015005 (2015)

184. H. F. Wen, Y. J. Li, E. Arima, Y. Naitoh, Y. Sugawara, R. Xu, and Z. H. Cheng, Investigation of tunneling current and local contact potential difference on the TiO_2 (110) surface by AFM/KPFM at 78 K, *Nanotechnol.* 28(10), 105704 (2017)

185. K. Chen, X. Wan, W. Xie, J. Wen, Z. Kang, X. Zeng, H. Chen, and J. Xu, Lateral built-in potential of monolayer MoS_2-WS_2 in-plane heterostructures by a shortcut growth strategy, *Adv. Mater.* 27(41), 6431 (2015)

186. Y. J. Yu, Y. Zhao, S. Ryu, L. E. Brus, K. S. Kim, and P. Kim, Tuning the graphene work function by electric field effect, *Nano Lett.* 9(10), 3430 (2009)

187. F. Long, R. Yasaei, R. Sanoj, W. T. Yao, P. Kral, A. Salehi-Khojin, and R. Shahbazian-Yassar, Characteristic work function variations of graphene line defects, *ACS Appl. Mater. Interfaces* 8(28), 18360 (2016)

188. C. Zheng, Q. Zhang, B. Weber, H. Ilatikhameneh, F. Chen, H. Sahasrabudhe, R. Rahman, S. Li, Z. Chen, J. Hellerstedt, Y. Zhang, W. H. Duan, Q. Bao, and M. S. Fuhrer, Direct observation of 2D electrostatics and ohmic contacts in template-grown graphene/WS_2 heterostructures, *ACS Nano* 11(3), 2785 (2017)

189. M. Precner, T. Polakovic, Q. Qiao, D. J. Trainer, A. V. Putilov, C. Di Giorgio, I. Cone, Y. Zhu, X. X. Xi, M. Iavarone, and G. Karapetrov, Evolution of metastable defects and its effect on the electronic properties of MoS_2 films, *Sci. Rep.* 8(1), 6724 (2018)

190. J. Shim, A. Oh, D. H. Kang, S. Oh, S. K. Jang, J. Jeon, M. H. Jeon, M. Kim, C. Choi, J. Lee, S. Lee, G. Y. Yeom, Y. J. Song, and J. H. Park, High-performance 2D rhenium disulfide (ReS_2) transistors and photodetectors by oxygen plasma treatment, *Adv. Mater.* 28(32), 6985 (2016)

191. R. Wang, S. N. Wang, D. D. Zhang, Z. J. Li, Y. Fang, and X. H. Qiu, Control of carrier type and density in exfoliated graphene by interface engineering, *ACS Nano* 5(1), 408 (2011)

192. V. Panchal, R. Pearce, R. Yakimova, A. Tzalenchuk, and O. Kazakova, Standardization of surface potential measurements of graphene domains, *Sci. Rep.* 3(1), 2597 (2013)

193. J. Li, X. Qi, G. Hao, K. Huang, and J. Zhong, Surface Potential of Graphene Oxide Investigated by Kelvin probe force microscopy, *Fuller. Nanotub. Carbon Nanostruct.* 23(9), 777 (2015)

194. G. Hao, Z. Huang, Y. Liu, X. Qi, L. Ren, X. Peng, L. Yang, X. Wei, and J. Zhong, Electrostatic properties of few-layer MoS_2 films, *AIP Adv.* 3(4), 042125 (2013)

195. X. Zhang, Q. Liao, S. Liu, Z. Kang, Z. Zhang, J. Du, F. Li, S. Zhang, J. Xiao, B. Liu, Y. Ou, X. Liu, L. Gu, and Y. Zhang, Poly(4-styrenesulfonate)-induced sulfur vacancy self-healing strategy for monolayer MoS_2 homojunction photodiode, *Nat. Commun.* 8, 15881 (2017)

196. C. Zheng, Z. Q. Xu, Q. Zhang, M. T. Edmonds, K. Watanabe, T. Taniguchi, Q. Bao, and M. S. Fuhrer, profound effect of substrate hydroxylation and hydration on electronic and optical properties of monolayer MoS_2, *Nano Lett.* 15(5), 3096 (2015)

197. T. H. Ly, H. Kim, Q. H. Thi, S. P. Lau, and J. Zhao, Superior dielectric screening in two-dimensional MoS_2 spirals, *ACS Appl. Mater. Interfaces* 9(43), 37941 (2017)

198. K. Zhang, T. Zhang, G. Cheng, T. Li, S. Wang, W. Wei, X. Zhou, W. Yu, Y. Sun, P. Wang, D. Zhang, C. Zeng, X. Wang, W. Hu, H. J. Fan, G. Shen, X. Chen, X. Duan, K. Chang, and N. Dai, Interlayer transition and infrared photodetection in atomically thin type-II $MoTe_2$ /MoS_2 van der Waals heterostructures, *ACS Nano* 10(3), 3852 (2016)

199. A. Verdaguer, M. Cardellach, J. J. Segura, G. M. Sacha, J. Moser, M. Zdrojek, A. Bachtold, and J. Fraxedas, Charging and discharging of graphene in ambient conditions studied with scanning probe microscopy, *Appl. Phys. Lett.* 94(23), 233105 (2009)

200. Y. S. Zhou, S. Wang, Y. Yang, G. Zhu, S. Niu, Z. H. Lin, Y. Liu, and Z. L. Wang, Manipulating nanoscale contact electrification by an applied electric field, *Nano Lett.* 14(3), 1567 (2014)

201. S. Kim, T. Y. Kim, K. H. Lee, T. H. Kim, F. A. Cimini, S. K. Kim, R. Hinchet, S. W. Kim, and C. Falconi, Rewritable ghost floating gates by tunnelling triboelectrification for two-dimensional electronics, *Nat. Commun.* 8, 15891 (2017)

202. T. Burnett, R. Yakimova, and O. Kazakova, Mapping of local electrical properties in epitaxial graphene using electrostatic force microscopy, *Nano Lett.* 11(6), 2324 (2011)

203. V. K. Sangwan, D. Jariwala, I. S. Kim, K. S. Chen, T. J. Marks, L. J. Lauhon, and M. C. Hersam, Gate-tunable memristive phenomena mediated by grain boundaries in single-layer MoS_2, *Nat. Nanotechnol.* 10(5), 403 (2015)

204. S. Luo, G. Hao, Y. Fan, L. Kou, C. He, X. Qi, C. Tang, J. Li, K. Huang, and J. Zhong, Formation of ripples in atomically thin MoS_2 and local strain engineering of electrostatic properties, *Nanotechnol.* 26(10), 105705 (2015)

205. G. Hao, L. Kou, D. Lu, J. Peng, J. Li, C. Tang, and J. Zhong, Electrostatic properties of two-dimensional WSe_2 nanostructures, *J. Appl. Phys.* 119(3), 035301 (2016)

206. S. Ghosh, W. Bao, D. L. Nika, S. Subrina, E. P. Pokatilov, C. N. Lau, and A. A. Balandin, Dimensional crossover of thermal transport in few-layer graphene, *Nat. Mater.* 9, 555 (2010)

207. S. E. Yalcin, C. Galande, R. Kappera, H. Yamaguchi, U. Martinez, K. A. Velizhanin, S. K. Doorn, A. M. Dattelbaum, M. Chhowalla, P. M. Ajayan, G. Gupta, and A. D. Mohite, Direct imaging of charge transport in progressively reduced graphene oxide using electrostatic force microscopy, *ACS Nano* 9(3), 2981 (2015)

208. G. L. Hao, X. Qi, J. Li, L. W. Yang, J. J. Yin, F. Lu, and J. X. Zhong, Surface potentials of few-layer graphene films in high vacuum and ambient conditions, *Solid State Commun.* 151(11), 818 (2011)

209. O. Kazakova, V. Panchal, and T. Burnett, Epitaxial graphene and graphene–based devices studied by electrical scanning probe microscopy, *Crystals* 3(1), 191 (2013)

210. S. H. Zhao, Y. Lv, and X. J. Yang, Layer-dependent nanoscale electrical properties of graphene studied by conductive scanning probe microscopy, *Nanoscale Res. Lett.* 6(1), 498 (2011)

211. H. Jeong, K. M. Lee, Y. H. Ahn, S. Lee, and J. Y. Park, Non-contact local conductance mapping of individual graphene oxide sheets during the reduction process, *J. Phys. Chem. Lett.* 6(13), 2629 (2015)

212. S. Hao, B. Yang, J. Yuan, and Y. Gao, Substrate induced anomalous electrostatic and photoluminescence properties of monolayer MoS_2 edges, *Solid State Commun.* 249, 1 (2017)

213. L. Jiang, B. Wu, H. Liu, Y. Huang, J. Chen, D. Geng, H. Gao, and Y. Liu, A general approach for fast detection of charge carrier type and conductivity difference in nanoscale materials, *Adv. Mater.* 25(48), 7015 (2013)

214. C. Tan, Y. Liu, H. Chou, J. S. Kim, D. Wu, D. Akinwande, and K. Lai, Laser-assisted oxidation of multi-layer tungsten diselenide nanosheets, *Appl. Phys. Lett.* 108(8), 083112 (2016)

215. Y. Liu, R. Ghosh, D. Wu, A. Ismach, R. Ruoff, and K. Lai, Mesoscale imperfections in MoS_2 atomic layers grown by a vapor transport technique, *Nano Lett.* 14(8), 4682 (2014)

216. P. J. d. Visser, R. Chua, J. O. Island, M. Finkel, A. J. Katan, H. Thierschmann, H. S. J. v. d. Zant and T. M. Klapwijk, Spatial conductivity mapping of unprotected and capped black phosphorus using microwave microscopy, *2D Mater.* 3(2), 021002 (2016)

217. J. S. Kim, Y. Liu, W. Zhu, S. Kim, D. Wu, L. Tao, A. Dodabalapur, K. Lai, and D. Akinwande, Toward air-stable multilayer phosphorene thin-films and transistors, *Sci. Rep.* 5(1), 8989 (2015)

218. V. V. Talanov, C. D. Barga, L. Wickey, I. Kalichava, E. Gonzales, E. A. Shaner, A. V. Gin, and N. G. Kalugin, Few-layer graphene characterization by near-field scanning microwave microscopy, *ACS Nano* 4, 3831 (2010)

219. C. J. Brennan, R. Ghosh, K. Koul, S. K. Banerjee, N. S. Lu, and E. T. Yu, Out-of-plane electromechanical response of monolayer molybdenum disulfide measured by Piezoresponse force microscopy, *Nano Lett.* 17(9), 5464 (2017)

220. Y. Zhou, D. Wu, Y. Zhu, Y. Cho, Q. He, X. Yang, K. Herrera, Z. Chu, Y. Han, M. C. Downer, H. Peng, and K. Lai, Out-of-plane piezoelectricity and ferroelectricity in layered a-In_2Se_3 nanoflakes, *Nano Lett.* 17(9), 5508 (2017)

221. M. J. Loiacono, E. L. Granstrom, and C. D. Frisbie, Investigation of charge transport in thin, doped sexithiophene crystals by conducting probe atomic force microscopy, *J. Phys. Chem. B* 102(10), 1679 (1998)

222. J. Nozaki, S. Mori, Y. Miyata, Y. Maniwa, and K. Yanagi, Local optical absorption spectra of MoS_2 monolayers obtained using scanning near-field optical microscopy measurements, *Jpn. J. Appl. Phys.* 55(3), 038003 (2016)

223. J. Nozaki, Y. Kobayashi, Y. Miyata, Y. Maniwa, K. Watanabe, T. Taniguchi, and K. Yanagi, Local optical absorption spectra of h-BN–MoS_2 van der Waals heterostructure revealed by scanning near-field optical microscopy, *Jpn. J. Appl. Phys.* 55(6S1), 06GB01 (2016)